

Sand transport processes and bed level changes induced by two alternating laboratory swash events

Joep van der Zanden^{a,*}, Iván Cáceres^b, Sonja Eichtopf^c, Jan S. Ribberink^a, Jebbe J. van der Werf^{d,a}, José M. Alsina^b

^a*Marine and Fluvial Systems group, University of Twente, Drienerlolaan 5, 7522 NB Enschede, Netherlands*

^b*Laboratori dEnginyeria Marítima, Universitat Politècnica de Catalunya, C. Jordi Girona, 1-3 08034 Barcelona, Spain*

^c*Department of Civil and Environmental Engineering, Imperial College London, South Kensington Campus, SW7 2AZ, UK*

^d*Deltares, P.O. Box 177, 2600 MH Delft, Netherlands*

Abstract

Sand transport processes and net transport rates are studied in a large-scale laboratory swash zone. Bichromatic waves with a phase modulation were generated, producing two continuously alternating swash events that have similar offshore wave statistics but which differ in terms of wave-swash interactions. Measured sand suspension and sheet flow dynamics show strong temporal and spatial variability, related to variations in flow velocity and locations of wave capture and wave-backwash interactions. Suspended and sheet flow layer transport rates in the lower swash zone are generally of same magnitude, but sheet flow exceeds the suspended load transport by up to a factor four during the early uprush. The bed level near the inner surf zone is relatively steady during a swash cycle, but changes of $\mathcal{O}(\text{cm/s})$ are measured near the mid swash zone where wave-swash interactions lead

*Corresponding author

Email address: vanderzandenjoep@gmail.com (Joep van der Zanden)

to strongly non-uniform flows. The two alternating swash events produce a dynamic equilibrium, with bed level changes up to a few mm induced by single swash events, but with net morphodynamic change over multiple events that is two orders of magnitude lower. Most of the intra-swash and the single-event-averaged bed level changes in the swash zone are caused by a redistribution of sediment within the swash. The transport of sediment across the surf-swash boundary is minor at intra-swash time scale, but becomes increasingly significant at swash-averaged time scales or longer (i.e., averaged over multiple swash events).

Highlights:

- Large-scale wave flume experiments involving two alternating bichromatic wave induced swash events.
- Sediment mobilization as sheet load and suspended load increases substantially from inner surf to lower swash zone.
- Sheet flow transport dominates the total transport during the early uprush and during instants of strong wave-backwash interactions.
- Single swash events can produce much greater net transport rates and bed level changes than the overall trend over multiple events.
- For the present conditions, the net sediment exchange between swash and surf zone is low and sediment is mainly redistributed within the swash.

Keywords: Swash zone, sediment transport, bed level change, wave groups, beach morphology, large-scale wave flume, sheet flow

1. Introduction

The swash zone is the part of the beach that is alternately inundated and exposed by the flow uprush and backwash. The combination of unsteady flows, high turbulence levels, large sediment transport rates and rapid bed level changes makes the swash a highly dynamic region (Masselink and Puleo, 2006; Brocchini and Baldock, 2008; Chardón-Maldonado et al., 2016). Processes in and near the swash zone ultimately determine whether sand is stored on the upper beach or transported offshore, hence controlling shoreline evolution. However, wave-averaged numerical models that are presently used in coastal engineering practice encounter great difficulties to accurately reproduce the morphologic evolution of the shoreline (van Rijn et al., 2013), which reflects a limited understanding of sand transport in the swash zone. Therefore, a better insight into the processes driving morphologic change in the swash is of vital importance to better understand and predict coastal erosion and sedimentation by natural processes or by human interferences.

A typical swash event consists of an uprush (incident wave running up a beach) and a backwash (run-down of the flow towards the sea). The hydrodynamics of single swash events, i.e., generated by solitary waves or dam breaks, have been extensively studied through experiments (e.g. Barnes et al., 2009; Kikkert et al., 2012, 2013; O’Donoghue et al., 2010; Pujara et al., 2015a; Higuera et al., 2018) and numerical simulations (e.g. Shen and Meyer, 1963; Hibberd and Peregrine, 1979; Barnes and Baldock, 2010; Briganti et al., 2011; Postacchini et al., 2014; Pintado-Patiño et al., 2015; Kim et al., 2017). During the uprush phase, the decelerating bore climbs the beach. The leading edge of the uprush bore is characterized by high bed shear stresses, which

26 relate to the limited time for development of the boundary layer (Kikkert
27 et al., 2012; Pintado-Patiño et al., 2015) and to the downward transport of
28 fluid with high landward momentum by the converging flow in the swash tip
29 (Barnes et al., 2009; Sou and Yeh, 2011; Baldock et al., 2014). The leading
30 edge of the uprush is further characterized by high turbulent kinetic en-
31 ergy, which dissipates rapidly after passage of the uprush bore (O’Donoghue
32 et al., 2010; Kikkert et al., 2012). After flow reversal, the flow accelerates
33 in seaward direction and the bed shear stress increases progressively as the
34 boundary layer develops. Free-stream velocities and bed shear stress reach
35 a maximum in seaward direction during the mid backwash, before the flow
36 decelerates during the final backwash stage.

37 The flow complexity increases for swash events driven by multiple waves,
38 where the arrival of successive waves at the beach can lead to wave-swash
39 interactions during uprush and backwash (Peregrine, 1974). A swash bore
40 overtaking a preceding bore during the uprush is typically termed “wave
41 capture” while an incident bore arriving during a preceding backwash leads
42 to a “wave-backwash interaction” (Hughes and Moseley, 2007; Cáceres and
43 Alsina, 2012). Wave-backwash interactions can be classified as “weak”, when
44 the incident wave has higher momentum than the backwash flow and con-
45 tinues to propagate towards the beach, or “strong”, when the incident wave
46 and backwash flow have similar momentum and the incident wave is halted
47 or washed seaward (Hughes and Moseley, 2007; Cáceres and Alsina, 2012;
48 Chen et al., 2016). Detailed observations and numerical simulations show
49 that such interactions lead to strong velocity shearing, flow separation and
50 vortex formation (Sou and Yeh, 2011; Pujara et al., 2015b; Chen et al., 2016;

51 Higuera et al., 2018).

52 On sandy beaches, the energetic flow conditions in the swash lead to the
53 transport of sediment as sheet flow and suspended load. The sheet flow layer
54 is the thin (up to a few cm thickness) layer of high sand concentration directly
55 above the non-moving bed, typically defined as the transport layer for which
56 intergranular and sediment-flow interaction forces are significant (Dohmen-
57 Janssen et al., 2001). Sediment grains lifted to higher elevations form the
58 suspended load. Recent swash measurements indicate that suspended and
59 sheet flow transport rates are of similar magnitude (Ruju et al., 2016; Puleo
60 et al., 2016; Wu et al., 2016). Depending on wave conditions, sand type, and
61 stage of the swash cycle, one transport mode may dominate over the other.

62 Sand suspension in the swash is not only controlled by local pick-up and
63 deposition but also by cross-shore advection (Kobayashi and Johnson, 2001;
64 Pritchard and Hogg, 2005; Alsina et al., 2009). Sediment pick-up in the
65 swash is associated with high flow speeds and turbulence levels (Osborne
66 and Rooker, 1999; Puleo et al., 2000; Aagaard and Hughes, 2006; Alsina and
67 Cáceres, 2011). The suspended sand concentration is maximum during the
68 early uprush, when both bed shear stress and turbulence levels are high,
69 and during the mid to late backwash stage, when flow velocities reach a
70 maximum in offshore direction (Osborne and Rooker, 1999; Butt and Russell,
71 1999; Masselink et al., 2005). Sand suspension has further been associated
72 with wave capture and wave-backwash interaction events that drive turbulent
73 mixing and pick-up from the bed (Hughes and Moseley, 2007; Cáceres and
74 Alsina, 2012; Alsina et al., 2012, 2018).

75 Sheet flow layer (SFL) dynamics have been extensively studied in oscil-

76 latory flow tunnels (Ribberink and Al-Salem, 1995; Hassan and Ribberink,
77 2005) and in wave flumes involving non-breaking (Dohmen-Janssen and Hanes,
78 2002, 2005; Schretlen, 2012) and breaking (Mieras et al., 2017; van der Zan-
79 den et al., 2017; Fromant et al., 2018) waves. In such conditions, sediment
80 is eroded from the bed and brought upward during maximum velocity mag-
81 nitudes, and settles when the velocity forcing reduces. As a result of this
82 predominantly local vertical sediment exchange, the SFL grows and decays
83 during each wave half cycle. Although the SFL in the swash exhibits sim-
84 ilar concentration distributions to observations under non-breaking waves
85 (Lanckriet et al., 2014; van der Zanden et al., 2015), its response to the free-
86 stream velocity is notably different. Firstly, because of the aforementioned
87 converging flows and boundary layer processes that affect the bed shear stress
88 during uprush and backwash. Secondly, additional forcing such as horizontal
89 pressure gradients, turbulence originating from swash bores, and wave-swash
90 interactions can enhance sediment mobilization and increase the SFL thick-
91 ness (Lanckriet and Puleo, 2015; van der Zanden et al., 2015). Thirdly, the
92 SFL dynamics are not only controlled by vertical processes but also by the
93 cross-shore sand advection within the swash (van der Zanden et al., 2015).
94 The latter is especially significant for narrow-band wave conditions that gen-
95 erate swash events with relatively high cross-shore excursion (Alsina et al.,
96 2018). Parameterizations for sheet flow layer thickness in the swash have
97 been presented (Lanckriet and Puleo, 2015), but the accurate simulation of
98 advection-dominated SFL dynamics and transport rates may require more
99 advanced advection-diffusion-type models (van der Zanden et al., 2015).

100 The high instantaneous and net sand transport rates in the swash have

101 been measured using sediment traps on natural beaches (Masselink and
102 Hughes, 1998; Jackson et al., 2004) and in laboratory flumes (O’Donoghue
103 et al., 2016; Alsina et al., 2009), or by inferring the net transport from ex-
104 posed bed level measurements (Blenkinsopp et al., 2011). Sediment loads and
105 transport rates are generally highest in the lower and mid swash zones, close
106 to the surf-swash boundary (Masselink and Hughes, 1998; Jackson et al.,
107 2004). Within a swash event, sediment is transported landward during the
108 uprush and seaward during the backwash. This cross-shore sand exchange
109 leads to bed level fluctuations at intra-swash time scales, as shown by field
110 measurements (Puleo et al., 2014), laboratory observations (Alsina et al.,
111 2018), and numerical model simulations (Zhu and Dodd, 2013, 2015; Ruffini
112 et al., 2019).

113 Net (i.e., swash-averaged) transport and bed level changes are generally
114 considered to result from an imbalance between the landward uprush and
115 seaward backwash transport. Net transport rates by different events within
116 one tidal cycle may vary strongly in terms of direction and magnitude, which
117 is partly attributed to wave-swash interactions that can enhance net trans-
118 port rates in either onshore or offshore direction (Weir et al., 2006; Hughes
119 and Moseley, 2007; Masselink et al., 2009; Blenkinsopp et al., 2011). Sev-
120 eral detailed numerical models have been developed to investigate the net
121 morphodynamic change by dam-break swash (e.g. Postacchini et al., 2012;
122 Zhu and Dodd, 2013) or swash events composed of multiple bores (Incelli
123 et al., 2016); a recent overview on swash zone morphodynamic models was
124 presented by Briganti et al. (2016).

125 Although many studies have been dedicated to understanding swash zone

126 morphodynamics, most previous experimental studies focused either on de-
127 tailed sand transport processes at few cross-shore locations, or on bulk statis-
128 tics of net transport rates in relation to wave conditions. The relation be-
129 tween intra-swash processes and swash-averaged sand transport rates and
130 morphologic change is, to a large extent, still unclear. This especially holds
131 for the more complex swash events that include wave-swash interactions.
132 This lack of process insights ultimately hampers the development of numer-
133 ical models for sand transport in the swash zone.

134 Therefore, the present study aims to improve insights into the effects of
135 intra-swash hydrodynamics and sediment transport processes on net bed level
136 change and sand transport rates. The specific research objectives are firstly
137 to study sand suspension and sheet flow layer processes near the shoreline,
138 and relate them to visual observations and measurements of the swash flow.
139 The second objective is to quantify bed level changes at intra-swash and
140 swash-averaged time scales and to relate them to the intra-swash processes.
141 The effects of different types of wave-swash interactions are of particular in-
142 terest. These processes are studied through experiments in a large-scale wave
143 flume which allows the generation of repeatable swash events. Compared to
144 previous laboratory experiments on this topic (van der Zanden et al., 2015;
145 Alsina et al., 2018), the present study offers more detailed measurements of
146 the sediment exchange between the surf-swash boundary and extends insights
147 on bed level changes and sand transport rates at different time scales (intra-
148 swash, swash-event averaged, and averaged over multiple swash events).

149 The experiment is described in Section 2. The overall bed profile evolution
150 is presented in Section 3. Section 4 presents the intra-swash hydrodynamic

151 and sediment transport processes, followed by the measured bed level changes
152 and sand transport rates (Section 5). The results are discussed in Section 6
153 and the main conclusions are presented in Section 7.

154 **2. Experiments**

155 *2.1. Experimental set-up*

156 The experiments were conducted in the large-scale CIEM wave flume at
157 the Universitat Politècnica de Catalunya, Barcelona, Spain. The flume is
158 approximately 100 m long, 3 m wide, and 4.5 m deep. Figure 1 shows the
159 experimental set-up. The water depth h near the wave paddle was 2.50 m.
160 The vertical coordinate z is defined positively upward from the still water
161 level (SWL) and the cross-shore coordinate x is defined positively landward
162 from the initial shoreline, the latter being calculated as the intersection be-
163 tween the SWL and the initial bed profile.

164 The beach profile consisted of medium sand with a median diameter D_{50}
165 = 0.25 mm, 10% and 90% cumulative intercepts $D_{10} = 0.15$ mm and D_{90}
166 = 0.37 mm, and a measured mean settling velocity $w_s = 0.034$ m/s. The
167 initial bed profile followed a 1:15 slope (Figure 1). In order to reduce cross-
168 flume flow and bed level asymmetries in the swash zone, the swash zone was
169 divided into three compartments with approximately same widths by means
170 of steel rectangular plates (“dividers”) along two cross-shore transects. The
171 0.70 m high, 6 m long dividers were buried approximately 0.40 m into the
172 initial bed and they extended over $x = 3.4$ to 9.4 m. A similar application of
173 dividers to reduce cross-tank bed asymmetry was adopted by Baldock et al.
174 (2017).

175 *2.2. Wave conditions*

176 The waves were generated at intermediate water depth by the wedge-
177 type wave maker. Steering signals for the wave paddle were based on first-
178 order wave theory. After building the bed profile, 30 min of irregular waves
179 with significant wave height $H_s = 0.42$ m and peak period $T_p = 4.0$ s were
180 produced in order to compact the bed. The experiment started with this
181 profile (experimental time $t = 0$).

182 After this, four 30-min and two 60-min consecutive hydrodynamic runs
183 were generated using bichromatic wave time series, yielding a total experi-
184 mental duration of 240 min (4 hours). Bichromatic waves result in repeatable
185 swash events, hence allowing for ensemble-averaging in order to increase the
186 accuracy of results, while they produce a similar morphologic development
187 as irregular waves (e.g. Baldock et al., 2011). An erosive and narrow-banded
188 bichromatic wave condition was selected, which was expected (based on previ-
189 ous experiments by Alsina et al., 2018) to result in energetic flow conditions,
190 strong wave-swash interactions, and relatively high cross-shore advection of
191 sediment.

192 The bichromatic waves in the present experiment had frequencies $f_1 =$
193 0.304 Hz and $f_2 = 0.236$ Hz and wave heights $H_1 = H_2 = 0.32$ m, correspond-
194 ing to a fully modulated wave group with group period $T_{gr} = \frac{1}{f_1 - f_2} = 14.8$ s
195 and a mean short wave period $T_m = \frac{2}{f_1 + f_2} = 3.7$ s.

196 Furthermore, the phase of the short waves within the groups was modu-
197 lated at a specified “repeat frequency”, which is defined as the frequency at
198 which a short wave phase within the group repeats exactly (Baldock et al.,
199 2000). This phase modulation allows to generate swash events that have the

200 same offshore wave height and peak period, but the different timing of the
201 short waves leads to variations in wave-swash interactions. For the present
202 experiment, the repeat period $T_R = 2T_{gr}$, hence resulting in two alternating
203 wave group induced swash events, termed A and B in what follows.

204 *2.3. Measurements*

205 An overview of the instruments is presented in Figure 1 and Table 1. A
206 combination of resistive wave gauges (RWGs), acoustic wave gauges (AWGs),
207 and pressure transducers (PTs) was deployed to measure the water surface
208 elevation η at various locations in the flume, covering the deeper section of
209 the flume up to the swash. All measurements of η were acquired at a sam-
210 pling frequency $f_s = 40$ Hz. The non-linear, weakly dispersive approach by
211 Bonneton et al. (2018) was applied to retrieve η from the pressure measure-
212 ments by the PTs. In the swash zone, the AWGs measured the water surface
213 elevation when the bed is submerged, or the bed level when it is exposed.
214 The measurement accuracy of the RWGs and PTs is estimated to be about 1
215 mm. The theoretical accuracy of the AWGs is 0.2 mm, except for the AWGs
216 at $x = 5.56$ and 6.51 m which have an accuracy of 0.02 mm (values provided
217 by the manufacturers of the commercial AWGs).

218 In order to quantify horizontal pressure gradients, additional measure-
219 ments of the water pressure at bed level were obtained using three PTs,
220 deployed around $x = 1.28$ m and separated by $\Delta x = 0.05$ m. These PTs
221 were orientated parallel to the bed, and were buried prior to each run such
222 that their top aligned with the local bed level.

223 The three-component flow velocity was measured at $f_s = 100$ Hz using
224 acoustic Doppler velocimeters (ADV) at five cross-shore locations, deployed

225 from the side-walls at a minimum distance of 0.3 m from the wall. All
226 Nortek ADVs were of a side-looking type and were deployed with a vertical
227 orientation of the ADV stems. This configuration minimizes flow disturbance
228 and facilitates measuring even at relatively shallow water depths. Prior to
229 each experimental run, all ADVs were vertically repositioned to 0.030 m
230 above the local bed level. The cross-shore velocity u is defined positively
231 landward.

232 Measurements of suspended sand concentrations were obtained at $f_s =$
233 40 Hz using five optical backscatter sensors (OBSs). The OBSs were de-
234 ployed from the side-walls at approximately the same locations as the ADVs
235 and were repositioned to 0.030 m above the local bed before each run. All
236 OBSs were calibrated at UPC for the present sediment, with a replica of the
237 calibration apparatus described by Downing and Beach (1989).

238 Sand concentrations in the SFL and the local bed level were measured at
239 two cross-shore locations using a conductivity-based concentration measure-
240 ment system, CCM⁺ (described in detail by van der Zanden et al., 2015).
241 The CCM⁺ system consists of two tanks that are buried into the bed. The
242 tanks contain up to three probes that can be vertically repositioned. The
243 probes enter the SFL from below, in order to minimize flow disturbance, and
244 measure the resistivity of the sediment-water mixture. The resistivity can
245 be translated to a concentration using a linear calibration, based on mea-
246 surements of the resistivity in the clear water and in the bed before each
247 experimental run. The measurement volume of each probe extends verti-
248 cally to 1-2 mm. The probes positions are continuously measured and can
249 be controlled with sub-mm accuracy using servomotors in the tanks. The

250 CCM⁺ system contains a bed level tracking mode in which the probes are
251 automatically repositioned to the elevation corresponding to the bed-water
252 interface or the middle of the SFL, hence also yielding a direct, continuous
253 measurement of the local bed level (more details are given by van der Zanden
254 et al., 2015).

255 The two CCM⁺ tanks were deployed near the initial shoreline (Figure 1b).
256 Tank 1 contains a single and a twin probe that consists of two sensors, spaced
257 1.5 cm in cross-shore direction. The latter can be used to measure particle
258 velocities in the sheet flow layer through cross-correlation (see McLean et al.,
259 2001, for more details). In the present experiment, the single probe was used
260 to measure the continuous bed level, while the twin probe measured SFL con-
261 centrations at various elevations around the evolving bed level. The latter
262 was achieved by adopting the procedure described by van der Zanden et al.
263 (2017), i.e., by alternating between 60-s intervals in a concentration measure-
264 ment mode (concentration measurements at varying, prescribed elevations,
265 covering a vertical range of ± 15 mm relative to the bed) and 15-s intervals
266 in the bed level tracking mode. A second CCM⁺ tank with one single probe
267 was buried 1.7 m offshore from tank 1. The control settings of the twin probe
268 (tank 1) were also applied for the single probe of tank 2. All CCM⁺ positions
269 and concentrations were sampled at $f_s = 1000$ Hz. Section 2.4 describes how
270 the SFL concentration field is reconstructed from the concentration and bed
271 level measurements.

272 The bed profile was measured at the start of the experiment and after
273 each experimental run, using the wheel bottom profiler described in Sánchez-
274 Arcilla and Cáceres (2017). The wheel profiler had 0.01 m vertical accuracy

275 and measured along the center line of the flume with 0.02 m cross-shore
276 resolution. Visual observations of the shoreline after each run were used
277 to ensure the profile measurements had the appropriate vertical reference
278 relative to the SWL. The maximum run-up and minimum run-down locations
279 were visually observed and noted down for each run. For some experimental
280 runs the swash flow was recorded on video.

281 *2.4. Data treatment*

282 All wave gauge and pressure measurements seaward from the shoreline
283 were vertically referenced with respect to the still water level at the start
284 of a run. All AWG measurements were de-spiked. Spectral analysis showed
285 that several AWG signals contained continuous spurious recordings with an
286 amplitude of 0.01 m and a frequency $f = 10$ Hz, likely due to an electric
287 distortion in their acquisition unit. These recordings were removed by a low-
288 pass filter with cut-off frequency $f = 8$ Hz. The AWG measurements in the
289 swash zone were converted into water depths by relating the water surface
290 elevation to the local, evolving bed. The exposed bed levels were obtained
291 from the AWG signal by using a moving minimum with a time window equal
292 to T_{gr} and were then cubically interpolated in time to obtain the evolving bed.

293 Spurious ADV measurements were identified as having a signal amplitude
294 (in digital counts) < 25 or a correlation value $< 50\%$. These recordings were
295 removed from the time series and not replaced. Phase-averaged velocities
296 were discarded for phase-averaged signal amplitudes < 50 . ADV and OBS
297 measurements were discarded for water depths $h < 0.05$ m, when the sensors
298 are exposed or very close to the water surface level.

299 The pressure measurements in the swash, used to measure the pressure

300 gradients, were first de-measured in order to remove any possible bias caused
301 by offsets in alignment with the bed. The measured pressure heads were then
302 converted to an absolute vertical reference by adding the local bed elevation
303 obtained from the bed profile measurements. Finally, the cross-shore pressure
304 gradient at $x = 1.28$ m was calculated from the most landward and most
305 seaward PTs (separated by $\Delta x = 0.10$ m) through central differencing.

306 All hydrodynamic and OBS measurements were phase-averaged follow-
307 ing the approach for wave groups that was presented by van der Zanden
308 et al. (2019) and that is shortly summarized here. Slight variations in the
309 timing of the short waves within each repeat cycle may lead to smoothen-
310 ing of the phase-mean when the data are directly phase-averaged over T_R
311 (van der Zanden et al., 2019). This effect was reduced by phase-referencing
312 (i.e., determine the zero crossings) and phase-averaging the data for each of
313 the short waves that form a T_R cycle, rather than directly over the full T_R
314 cycle. The phase averages of the short waves were then merged to obtain a
315 phase average at the T_R cycle. Only data of the last two hydrodynamic runs
316 (two hours) were used for phase-averaging, assuming that a quasi-equilibrium
317 morphological equilibrium has established at that time (see Section 3 for the
318 profile evolution, and Alsina et al. (2016, 2018) for information on beach pro-
319 file variability under bichromatic wave conditions). For each run, the first
320 five minutes of data were discarded. The phase averages are time-referenced
321 such that $t/T_{gr} = 0$ corresponds to the arrival of the first wave of wave group
322 A at the location of CCM⁺ tank 2 (unless stated differently).

323 The CCM⁺ measured concentrations at various elevations around the
324 evolving bed. As a first processing step, the continuous bed level $z_{bed}(t)$ at the

325 locations of both tanks was reconstructed by a temporal cubic interpolation
 326 of the direct bed level measurements by the CCM⁺ (i.e., when in bed level
 327 tracking mode). This allowed the known probe elevation $z_{\text{probe}}(t)$ with respect
 328 to the top of the tank to be vertically referenced with respect to the evolving
 329 bed level, yielding a relative probe elevation $z'(t) = z_{\text{probe}}(t) - z_{\text{bed}}(t)$. The
 330 CCM⁺ concentration measurements $C(z', t)$ were then phase-averaged and
 331 at the same time vertically bin-averaged using a bin size $\Delta z' = 0.5$ mm.
 332 This ultimately resulted in phase-averaged concentration profiles $C(z', t/T_{\text{gr}})$
 333 in the sheet flow layer (for more details about the CCM⁺ data processing
 334 methodology, the reader is referred to van der Zanden et al., 2015, 2017).
 335 The CCM⁺ data were averaged over the last two hours of experiments, cor-
 336 responding to approximately 240 swash repetitions.

337 Sediment particle velocities in the sheet flow layer were obtained using
 338 the cross-correlation method described by McLean et al. (2001). The method
 339 estimates particle velocities based on the time lag that a turbulent cloud of
 340 particles requires to travel between two sensors aligned in cross-shore di-
 341 rection. In the present study, the high-pass filtered (1 Hz cut-off frequency)
 342 concentration measurements by the two sensors of the twin probe were cross-
 343 correlated for time intervals $\Delta t = 0.3$ s, corresponding to 100 phases in the
 344 T_{R} cycle. The cross-correlation output was phase-averaged and bin-averaged
 345 over concentration bins with $\Delta C = 0.1$ m³/m³. The averaging over concen-
 346 tration bins facilitates the calculation of particle velocities at different eleva-
 347 tions (corresponding to concentration levels) in the sheet flow layer. Finally,
 348 the time lag corresponding to the maximum phase-averaged cross-correlation
 349 output is used to calculate the phase-averaged particle velocity $u_{\text{p}}(t)$.

350 **3. Bed profile evolution**

351 Figure 2a shows the bed profile evolution during the experiment. The
352 bed profile evolves rapidly during the first 120 min. Prominent morphologic
353 features that are formed include a berm ($x = 6 - 10$ m) and a breaker bar
354 (crest at $x = -10$ m). During these first two hours, the shoreline retreats
355 by 1.8 m. During the remainder of the experiment ($t = 120$ to 240 min),
356 the profile rate of change is much lower. The breaker bar and trough move
357 gradually offshore, while the swash berm shows little further development.
358 The shoreline continues to erode (by 0.5 m), but with much smaller rates of
359 change than during the first two hours. Based on this morphologic evolution,
360 the bed profile between $t = 120$ and 240 min is considered to be in a quasi-
361 equilibrium state in which the bed level change is assumed to have a negligible
362 effect on the hydrodynamic and sediment transport processes of interest.

363 The net total sand transport rate q_{tot} can be calculated from the bed
364 profile rate of change $\Delta z_{\text{b}}/\Delta t$ by solving a mass balance equation (Exner
365 equation):

$$q_{\text{tot}}(x_i) = q_{\text{tot}}(x_{i-1}) - \int_{x_{i-1}}^{x_i} \rho_s(1-p) \frac{\Delta z_{\text{b}}}{\Delta t} dx \quad (1)$$

366 where $p = 0.4$ is the porosity of the loosely packed sand and $\rho_s = 2650$
367 kg/m^3 is the sediment density. Equation 1 is solved numerically, starting from
368 the landward end of the profile where $q_{\text{tot}} = 0$. Figure 2b shows the mean
369 q_{tot} for each experimental hour. Net total transport magnitudes are highest
370 in the first hour. During the first hour the swash berm is largely formed
371 by landward transport at $x > 0$ m while the seaward transport at $x < 0$ m
372 contributes to the breaker bar formation. The transport rates decrease as the

373 bed profile evolves. During the last two hours (120 – 240 min) the transport
374 at the berm ($x > 5$ m) is minor, while a gradual, seaward-directed transport
375 persists around the initial shoreline ($x = 0$ m).

376 For a more detailed analysis of the bar formation and shoreline evolution
377 during the experiment, the reader is referred to Eichertopf et al. (2019).

378 **4. Intra-swash hydrodynamics and sand transport processes**

379 This section presents an overview of the hydrodynamics (Section 4.1),
380 followed by the measurements of sand suspension, sheet flow layer dynamics,
381 and intra-swash sand transport rates (sections 4.2, 4.3, and 4.4, respectively).

382 *4.1. Hydrodynamics*

383 *4.1.1. Wave evolution*

384 In this section the water surface elevation in time and space is studied.
385 The mean variability (averaged over time and over all locations) in phase-
386 ensembles of the water surface elevation is 0.006 m (i.e., $\ll H_1, H_2$). This
387 indicates a good repeatability of the generated wave groups and swash events.

388 The wave evolution along the flume is illustrated in Figure 3. Figure
389 3a-c shows the phase-averaged water surface elevation at three cross-shore
390 locations. In this representation, the time series are phase-referenced such
391 that t/T_{gr} corresponds to the start of the T_{R} cycle at each location.

392 Near the wave paddle ($x = -63.4$ m) the two wave groups together
393 consist of approximately seven short waves that are roughly sinusoidal in
394 shape and that are of similar wave period. The significant wave height is
395 similar for both groups, but the timing of the short waves varies slightly.

396 At $x = -15.7$ m, just before outer wave breaking, the wave group structure
397 has remained similar while the wave height and skewness have increased
398 considerably. In the inner surf zone ($x = -3.4$ m), the wave height has
399 decreased due to energy losses at breaking and the short waves have a pitched
400 forward, sawtooth-shape. The seven short waves can still be identified, but
401 the higher waves have shifted forward in phase within the group. This form
402 of amplitude dispersion, termed “wave focusing”, occurs at intermediate and
403 shallow water depths and is explained by a higher propagation speed of the
404 short waves that travel at the crest of the long wave (van Dongeren et al.,
405 2007; Tissier et al., 2015; Padilla and Alsina, 2017).

406 Figure 3d shows the cross-shore distribution of the maximum wave height
407 H_{\max} , calculated here as the difference between minimum and maximum
408 phase-averaged η . The wave height is roughly constant over the deeper sec-
409 tion of the flume and increases over the sloping bed. Visual observations
410 show that wave breaking occurred at $x = -10$ m for the larger waves and at
411 -5.5 m for the smaller waves, which corresponds to the region of decreasing
412 H_{\max} .

413 For the present bichromatic waves, wave shoaling and breaking is ex-
414 pected to not only lead to a transfer of energy to the higher harmonics but
415 also to the group-bound and breakpoint-generated forced long waves (Bal-
416 dock et al., 2000; Janssen et al., 2003; Lara et al., 2011; Padilla and Alsina,
417 2017). The energy at short- and long-wave frequencies is examined by de-
418 compositing the phase-averaged water surface elevation into a high-frequency
419 (η_{hf}) and low-frequency (η_{lf}) component, using an 8th-order Butterworth fil-
420 ter with 0.1 Hz cut-off frequency.

421 Figure 3e shows the root-mean-square (rms) of both components. The
422 low-frequency component $\eta_{\text{lf,rms}}$ increases from the wave paddle up to outer
423 wave breaking, consistent with an energy transfer from the short waves to the
424 bound long wave. The low-frequency wave energy decreases in the surf and
425 swash zones, but not as rapidly as the energy at the short-wave frequencies.
426 As a result, $\eta_{\text{lf,rms}}$ exceeds $\eta_{\text{hf,rms}}$ around the shoreline and in the swash. A
427 clear pattern of cross-shore modulations is observed for $\eta_{\text{lf,rms}}$, marking the
428 nodes ($x = -22$ and -3.5 m) and anti-nodes ($x = -32$, -11 , and 0.5 m) of
429 a quasi standing wave. This standing wave pattern is highly similar to mea-
430 surements by Alsina et al. (2016) and is explained by the linear superposition
431 of the incident bound long and outgoing reflected and breakpoint-generated
432 free long waves (Baldock et al., 2000; Baldock, 2006; Padilla and Alsina,
433 2018).

434 The energy transfer to long-wave frequencies may be explained by two
435 mechanisms: (i) the nonlinear coupling of primary wave components (Longuet-
436 Higgins and Stewart, 1962); (ii) breakpoint generation of the long wave
437 (Symonds et al., 1982). The dominance of either mechanism can be pre-
438 dicted using empirical parameters, e.g., the normalized beach slope (Battjes
439 et al., 2004) or the surf beat similarity parameter (Baldock, 2012). Based
440 on both parameters, the present experiment corresponds to a steep-slope,
441 steep-wave regime in which the breakpoint generation mechanism dominates
442 over the nonlinear growth mechanism.

443 The propagation of wave groups in the surf and swash regions is further
444 illustrated in Figure 4 which shows the high (Figure 4a) and low frequency
445 (Figure 4b) phase-averaged water surface elevation along the flume as con-

446 tour plots. The phasing of the individual waves forming the groups clearly
447 determines the swash events and the degree of interaction between shoreline
448 oscillation and successive arriving waves (next section). The quasi standing
449 pattern of $\eta_{lf}(t)$ is clearly seen in Figure 4b, with nodes and anti-nodes corre-
450 sponding to the descriptions of Figure 3e. Similar patterns of $\eta_{lf}(t)$ have been
451 observed in previous experimental (Padilla and Alsina, 2018) and numerical
452 (e.g. Brocchini and Peregrine, 1996) studies. The low frequency motion af-
453 fects the swash motion as the shoreline oscillation correlates positively with
454 $\eta_{lf}(t)$ and because it affects the short-wave celerity in shallow water (Tissier
455 et al., 2015; Padilla and Alsina, 2017).

456 4.1.2. *Description of swash events*

457 The swash events are first qualitatively discussed using the photo series
458 in Figure 5. The top panel shows the water depth at the location of CCM⁺
459 tank 1 and includes phase reference to the photos (marks a-j). The photos
460 are snapshots from a video recording, obtained from the upper swash zone
461 facing in seaward direction. The swash dividers are seen in the lower half of
462 each photo. The bottom of the photos corresponds to $x \approx 4$ m, the black
463 dashed line marks the location of CCM⁺ tank 1 ($x = 1.28$ m). The photos
464 illustrate the stepwise evolution of the swash events:

- 465 a) The first bore of swash event A has just reached the initial shoreline
466 location. Two bores (a small one, followed by a larger one) can be
467 observed just seaward of CCM⁺ tank 1.
- 468 b) The second bore has a higher propagation speed than the first bore,
469 possibly because it travels on the crest of the long wave (see Figure 4).

470 The second bore has almost overtaken the first bore and both bores
471 have passed CCM⁺ tank 1 with a minor time delay. The water depth
472 (top panel) increases in two steps, first at $t/T_{\text{gr}} = 0.08$ (arrival of the
473 first bore) and then at $t/T_{\text{gr}} = 0.13$ (arrival of the second bore). The
474 overtaking of the first bore by the second, termed “wave capture” fol-
475 lowing Hughes and Moseley (2007), occurs at $x = 1.5$ m (just landward
476 of CCM⁺ tank 1). The two merged bores generate a large run-up.

477 c) In the mid swash (bottom half of photo), the backwash has started
478 and the velocity is seaward directed. A third incident bore propagates
479 towards the swash zone (upper arrow in photo).

480 d) The third incident bore is retarded by the seaward momentum of the
481 backwash. The incident bore passes the CCM⁺, but is then fully halted
482 at $x \approx 1.8$ m, leading to a stationary bore that is similar to a hydraulic
483 jump (“strong wave-backwash interaction”, after Hughes and Moseley,
484 2007). The photo shows a high suspended sand load in the stationary
485 bore.

486 e) The stationary bore is washed seaward during the remainder of the
487 backwash stage. A next bore (first bore of event B) is observed in the
488 inner surf zone.

489 f) The start of swash event B. The first bore in event B has been slowed
490 down by the momentum of the preceding backwash of event A. A second
491 incident bore has almost overtaken the first bore of event B.

492 g) The second bore of event B overtakes and merges with the first bore.

493 This occurs at $x \approx -1$ m, which is approximately 2 m seaward of
494 CCM⁺ tank 1. The merged bore has a steep front, leading to a sudden
495 rise in water depth at the location of CCM⁺ tank 1 (upper panel,
496 $t/T_{\text{gr}} = 1.10$).

497 h) The merged bore produces a run-up that is lower than for event A. A
498 third bore of wave group B is observed in the inner surf zone.

499 i) The third bore arrives to the swash. The bore has higher momentum
500 than the retreating backwash and it continues to propagate landward
501 (“weak wave-backwash interaction”, Hughes and Moseley, 2007), pro-
502 ducing a second uprush within swash event B. The run-up is followed
503 by a long, uninterrupted backwash.

504 j) A fourth, small bore arrives to the swash. The bore has little momen-
505 tum and dissipates near the initial shoreline (marked by “=” in the
506 photo). The swash front of this bore does not reach CCM⁺ tank 1.
507 The first bore of event A can be seen in the inner surf zone (marked
508 by arrow).

509 A more quantitative illustration of the swash events is shown in Figure 6a
510 (AWG measurements). The boundary between the swash zone and the inner
511 surf zone was established from visual observations of the minimum run-down
512 location ($x = -0.9$ m). The maximum run-up, produced by events of type
513 A, was visually observed to reach $x = 9.9$ m, hence the total swash excursion
514 is 10.8 m. Following definitions by Aagaard and Hughes (2006), the lower
515 (> 75 % immersion), mid (> 40 , < 75 % immersion) and upper (< 40 %
516 immersion) swash zones are distinguished (Figure 6b).

517 Figure 6a shows the large uprush generated by the two first bores of event
518 A. The third bore (arriving to the lower swash around $t/T_{\text{gr}} = 0.4$) does not
519 produce another major uprush event but is instead halted at $x = 1.8$ m
520 ($t/T_{\text{gr}} = 0.6$). Swash event B generates a first uprush with a maximum
521 location of $x = 5.5$ m, which is considerably lower than for the uprush by
522 event A ($x = 9.9$ m). This implies that the incident momentum of the two
523 first bores at the shoreline is higher for event A than for event B. The third
524 incident bore of event B arrives to the initial shoreline around $t/T_{\text{gr}} = 1.25$
525 and produces another run-up, with a similar maximum location ($x = 6.0$ m)
526 as the first run-up of this event.

527 *4.1.3. Flow velocity*

528 The cross-shore flow velocity u measured by the ADVs at $z - z_{\text{bed}} = 0.03$
529 m is shown for three cross-shore locations in Figure 6b. For the interpretation
530 it should be noted that fluid velocities in the swash are depth-variable, with
531 boundary layers that can reach up to the water surface (Pintado-Patiño et al.,
532 2015). For the present study, assuming a roughness $k_s = 3D_{90}$ (Hughes,
533 1995), the bed would be classified as hydraulically smooth following Jonsson
534 (1980). For such smooth beds and for similar velocity magnitudes as the
535 present study's, O'Donoghue et al. (2010) observed that swash velocities
536 are approximately depth-uniform above a near-bed layer that reaches up to
537 about 0.02 m. Consequently, the ADV-measured velocities at $z - z_{\text{bed}} =$
538 0.03 m can be considered a reasonable proxy for the depth-averaged velocity.
539 The velocities can be directly related to the water depths, shown as colour
540 contour in the background of Figure 6b.

541 High landward velocities are observed at the front of event A's uprush

542 ($t/T_{\text{gr}} = 0 - 0.2$). The velocity at $x = -1.54$ and 0.27 m increases in
543 two steps, due to the two bores arriving shortly after each other, whereas it
544 increases at once at $x = 2.26$ m, where the bores have merged. Comparing the
545 maximum velocity at the three cross-shore locations shows that the uprush
546 flow accelerates between $x = -1.54$ and 0.27 m (inner surf to lower swash),
547 reaching a maximum of 1.6 m/s, and decelerates towards $x = 2.26$ m (lower
548 swash to mid swash).

549 The backwash flow of event A ($t/T_{\text{gr}} = 0.3 - 0.95$) is strongly cross-shore
550 non-uniform. The backwash flow at $x = 2.26$ m increases progressively in
551 magnitude, reaching values up to -2 m/s. The seaward-directed velocity at
552 $x = 0.27$ m increases after flow reversal ($t/T_{\text{gr}} = 0.30 - 0.43$), but then it
553 decreases due to the arrival of the third incident bore that induces the strong
554 wave-backwash interaction. Comparison of the velocity at the three locations
555 indicates the high non-uniformity of the cross-shore flow at this stage of the
556 swash cycle ($t/T_{\text{gr}} \approx 0.43$). Velocities at $x = 0.27$ m are seaward-directed
557 while the third incident bore passes and continues to propagate landward.
558 This likely marks a strong vertical shear distribution of u , with seaward-
559 directed velocities near the bed (as measured by the ADV at $z - z_{\text{bed}} = 0.03$
560 m) and landward-directed velocities higher in the water column. Such a
561 vertical structure of the cross-shore flow with seaward- and landward-directed
562 constituents would be consistent with previous measurements of the flow in
563 case of strong wave-backwash interactions (Chen et al., 2016; Pujara et al.,
564 2015b). The remainder of the backwash is characterized by quasi-steady
565 velocities of about -0.6 m/s at $x = 0.27$ m and -1 m/s at $x = -1.54$ m.

566 The first uprush of event B (starting at $t/T_{\text{gr}} = 0.95$) is formed by two

567 bores that merge in the inner surf zone. Maximum u during the uprush
568 is approximately 1 m/s for each location. The third bore (inducing the
569 weak wave-backwash interaction) arrives at $t/T_{\text{gr}} = 1.2 - 1.3$, just when the
570 backwash stage induced by the first uprush is about to begin, and leads to a
571 short-duration reversal to landward flow of small magnitude. The backwash
572 flow increases gradually in magnitude at $x = 2.26$ m, while it is quasi-steady
573 at $x = 0.27$ m.

574 Comparison of the two events shows that the higher maximum run-up for
575 event A is explained by a higher uprush velocity and landward momentum
576 flux in the lower swash. The difference in maximum run-up between the two
577 events relates further to the relatively high seaward-directed velocities in the
578 inner surf zone ($x = -1.54$ m, $t/T_{\text{gr}} = 0.6 - 0.9$) for event A, which causes
579 stronger retardation of the incident bores of event B. The latter also explains
580 why the two first bores merge further seaward for event B than for event A.

581 *4.2. Sediment suspension*

582 Several studies have been dedicated to sediment suspension in the swash
583 zone (e.g., Butt and Russell, 1999; Osborne and Rooker, 1999; Aagaard and
584 Hughes, 2006; Cáceres and Alsina, 2012, 2016). The results in this section
585 serve mainly to provide a coherent view on sand transport processes during
586 the present experiment.

587 The temporal and cross-shore variation in suspended sand concentration,
588 measured by OBSs at $z - z_{\text{bed}} = 0.03$ m, is shown in Figure 7. This fig-
589 ure shows the water depth (Figure 7a), cross-shore velocity (Figure 7b) and
590 suspended sand concentration (Figure 7c) at three cross-shore locations (in-
591 ner surf, lower swash, and mid swash). The water depth and velocity were

592 discussed in the previous sections and are here shown for reference.

593 The temporal variation in C is relatively small at $x = -1.68$ m (inner
594 surf zone), but it increases progressively towards the lower ($x = 0.38$ m) and
595 mid ($x = 2.36$ m) swash zone. Peaks in suspended sand concentration are
596 observed during the uprush of both events, with maximum C being reached
597 shortly after the velocity has reached its maximum. The concentration peak
598 at $x = 0.38$ m around $t/T_{\text{gr}} = 0.60$, shortly after arrival of the third bore
599 ($t/T_{\text{gr}} = 0.50$), is attributed to a horizontal influx of suspended sediment
600 from the landward side, where the strong wave-backwash interaction induced
601 by the third bore (at $x = 1.8$ m) drives turbulent mixing and pick-up of
602 sediment from the bed. This explanation is supported by other studies that
603 have addressed the significant effect of strong wave-backwash interactions on
604 sand suspension (Hughes and Moseley, 2007; Cáceres and Alsina, 2012). The
605 peaks in C at $x = 2.36$ m around $t/T_{\text{gr}} = 0.58$ and at $x = 0.38$ m around
606 $t/T_{\text{gr}} = 1.75$ are probably related to the high flow velocity during the final
607 backwash stages.

608 For both events, the suspended sand concentration C varies by up to an
609 order of magnitude between the different cross-shore locations. The maxi-
610 mum C during the uprush increases progressively from the inner surf to the
611 lower swash to the mid swash zone, even though the maximum uprush ve-
612 locity remains of similar magnitude or even decreases over x . This indicates
613 that the high suspended sand concentration at the turbulent swash front is
614 probably not only due to local re-suspension at the front, but in addition,
615 due to landward advection of the suspended load that is kept in suspension.
616 This leads to a progressive increase in the suspended load at the swash front

617 as it propagates landward (as also shown by Alsina et al. (2018) for similar
618 swash conditions). Also the confining water depth from inner surf to swash
619 zone may contribute to the increase in C .

620 The uprush concentrations are substantially higher for swash event B,
621 despite generally lower uprush velocities than for event A. This is attributed
622 to the differences in the location of wave capture between events A (wave
623 capture at $x \approx 1.5$ m) and B (at $x \approx -1$ m). The uprush of event A consists
624 in the lower swash of a small incident bore that precedes the larger, main
625 bore, and which reduces the impact of the main bore on the bed. On the
626 other hand, the uprush of event B consists in the lower swash of a single,
627 relatively large bore that propagates directly over the exposed bed and which
628 is therefore expected to induce high bed shear stresses (Barnes et al., 2009;
629 Sou and Yeh, 2011; Kikkert et al., 2012).

630 *4.3. Sheet flow dynamics*

631 *4.3.1. Sheet flow layer concentrations and thickness*

632 The CCM⁺ concentration measurements in the sheet flow layer (SFL)
633 were phase-averaged and vertically bin-averaged over 218 repeating T_R cycles
634 following the procedures described in Section 2.4. Figure 8 shows the phase-
635 averaged volumetric concentrations around the swash-averaged bed level,
636 $C(z', t/T_{gr})$, normalized by the concentration in the bed ($C_{bed} = 1 - p = 0.6$
637 m^3/m^3) for two phases. These phases were selected as they correspond to
638 well-developed sheet flow layers, hence clearly illustrating the vertical struc-
639 ture of the concentration profile. The measured sand concentrations (white
640 circles) approach an upward concave distribution. Despite the phase- and
641 bin-averaging, the scatter in the data is considerable. This is especially at-

642 tributed to the uncertainty in the measurement of $z_{\text{bed}}(t)$, and consequently,
 643 in $z'(t)$, which is estimated to be $\approx 2 - 4$ mm. Such small variability is
 644 sufficient to cause significant scatter in $C(z')$ distributions over a SFL with
 645 $\mathcal{O}(\text{mm to cm})$ thickness.

646 In order to reduce any effects of the variability in $C(z')$ on the esti-
 647 mated SFL thickness, the empirical model for concentration distributions by
 648 O'Donoghue and Wright (2004a) is fitted to the data:

$$C(z', t) = C_{\text{bed}} \frac{\beta(t)^\alpha}{\beta(t)^\alpha + [z' + \delta_e(t)]^\alpha} \quad (2)$$

649 In this equation α and β are shape parameters; δ_e is the SFL erosion
 650 depth that defines the bottom boundary of the curve. A fixed value of
 651 $\alpha = 1.5$ is used for the present study (based on O'Donoghue and Wright,
 652 2004a). Previous measurements of $C(z')$ in the swash agreed well with Equa-
 653 tion 2 (Lanckriet et al., 2014; van der Zanden et al., 2015), which justifies
 654 the equation's applicability to the present data. The values for β and δ_e
 655 are determined by fitting Equation 2 to the log-transformed concentration
 656 measurements using a least-square fitting approach. Similar curve fitting to
 657 CCM⁺ measurements in the swash was done by van der Zanden et al. (2015)
 658 and Alsina et al. (2018). Their approach is followed closely, except that the
 659 concentration measurements and the model were transformed by taking the
 660 logarithms prior to fitting. This reduces the bias of the fitted curve to high
 661 concentrations (lower SFL) and improves the fit in the upper SFL. The coef-
 662 ficient of determination (r^2) was 0.68 ± 0.12 for CCM⁺ tank 1 and 0.82 ± 0.07
 663 for tank 2.

664 Figure 8 shows the obtained fits (solid line) to the measured concentra-

665 tions. The grey circle marks the SFL “pivot point” z_p , which is the elevation
 666 around which the concentration profile pivots as the SFL grows and decays
 667 during a wave or swash cycle and which corresponds approximately to the
 668 middle of the sheet flow layer (O’Donoghue and Wright, 2004a). The figure
 669 also indicates the SFL thickness δ_s , i.e., the distance between the top and
 670 bottom of the SFL, with the top defined as the elevation where $C/C_{\text{bed}} = 0.12$
 671 (Dohmen-Janssen and Hanes, 2002).

672 The SFL concentrations are shown in Figure 9d,e. For reference, the figure
 673 includes the local water depths (a), cross-shore pressure gradients (b) and
 674 cross-shore velocities (c). The pressure gradients $-dp/dx$, computed at $x =$
 675 1.28 m, are negative (“seaward dipping”) during most of the swash cycle, with
 676 short-duration positive $-dp/dx$ peaks (“landward dipping”) during incident
 677 bore arrivals. The pressure gradients in positive and negative direction are of
 678 similar magnitude and the patterns are consistent with previous observations
 679 (Baldock and Hughes, 2006; Othman et al., 2014) and numerical simulations
 680 (Torres-Freyermuth et al., 2013). The concentration field in Figure 9d,e
 681 represents the fitted concentrations (Equation 2). The white areas in the
 682 figure correspond to measurements above the water surface. The white lines
 683 mark the bottom and top of the SFL and the black line marks the pivot
 684 point elevation. Figure 9f shows the SFL thickness (δ_s) at both locations.

685 At $x = -0.52$ m (Figure 9d) the concentration field is approximately
 686 steady, indicating little SFL development, throughout event A. As soon as
 687 the uprush of event B starts ($t/T_{\text{gr}} = 0.99$), the sheet flow layer grows rapidly,
 688 leading to a vertical dilution of the concentration field. As soon as the swash
 689 front has passed, the SFL reduces in thickness ($t/T_{\text{gr}} = 1.05 - 1.20$). The bed

690 remains more or less at rest until the SFL expands and decreases again during
691 the late backwash ($t/T_{\text{gr}} = 1.8 - 2.0$). The bed experiences a local erosion
692 during the uprush of event B, as shown by the decreasing pivot elevation
693 ($t/T_{\text{gr}} = 1.0-1.2$), while it is restored during the late backwash stage ($t/T_{\text{gr}} =$
694 $1.8 - 2.0$). These intra-swash bed level changes are explored in Section 5.1.

695 The SFL behaviour at $x = 1.28$ m is more dynamic than at $x = 0.52$
696 m (Figure 9e,f). At the swash front of both events A and B ($t/T_{\text{gr}} = 0.10$
697 and 1.05) the SFL grows rapidly, followed by a gradual decrease during the
698 remainder of the uprush. Another large increase in SFL thickness occurs
699 between $t/T_{\text{gr}} = 0.67 - 0.74$. This is shortly after the third incident bore
700 has passed and has interrupted the backwash flow, leading to u close to 0
701 m/s (Figure 9a,c). The initiation of sheet flow can be predicted based on
702 the mobility parameter $\psi = u^2/[(s - 1)gD_{50}]$, where $s = 2.65$ (-) is the
703 relative sediment density and $g = 9.81$ m/s² is the gravitational acceleration.
704 Following van Rijn (2007), the initiation of sheet flow is expected for $\psi > 250$,
705 which corresponds for the present sediment to $u > 1$ m/s. Consequently,
706 it is unlikely that the observed low velocity magnitudes induce sufficiently
707 high bed shear stresses to mobilize the sand and explain the growth in SFL
708 thickness. Instead, the increase is likely due to a horizontal influx of sediment
709 originating from landward locations: this sediment is mobilized by the strong
710 wave-backwash interaction at $x = 1.8$ m (about 0.5 m landward of these
711 CCM⁺ observations) at $t/T_{\text{gr}} = 0.6$; seaward advection of the sheet load
712 drives the observed increase in δ_s at $x = 1.28$ m during $t/T_{\text{gr}} = 0.67 - 0.74$.
713 The latter explanation is supported by observations of van der Zanden et al.
714 (2015) that revealed the significant mobilization of sediment as sheet load by

715 strong wave-backwash interactions.

716 At both locations, the uprush of event B mobilizes more sediment as sheet
717 flow than event A, even though uprush velocities are of similar magnitude.
718 Note that also the suspended sand concentration was substantially higher
719 for the uprush of event B than for event A. Both results indicate a larger
720 sediment mobilization for uprush B, which is explained by the structure of the
721 uprush: a large bore preceded by a small bore for event A, a large “merged”
722 bore propagating over an exposed bed for event B. The direct impact on the
723 bed is expected to be higher for event B (as also addressed in Section 4.2).

724 Comparison of these two lower swash zone locations shows that the up-
725 rush SFL thickness is greater at $x = 1.28$ m than at $x = -0.52$ m, despite
726 similar uprush velocity. This could be explained by landward advection of
727 the mobilized sediment in the SFL, leading to a gradually increasing sheet
728 load at the propagating swash front. Another explanation could be that
729 the turbulent energy, which has been suggested to contribute significantly to
730 SFL development (Lanckriet and Puleo, 2015), increases from $x = -0.52$ m
731 to $x = 1.28$ m.

732 Comparison of Figure 9b and e does not reveal any evident relation be-
733 tween the SFL behaviour and the measured cross-shore pressure gradients at
734 $x = 1.28$ m. The peaks of the pressure gradients during the two uprush events
735 A and B are of similar magnitude and do not explain the differences in SFL
736 thickness. The peaks of the positive pressure gradient during the third bore
737 arrival within each event ($t/T_{\text{gr}} = 0.54$ and 1.30) induce no evident SFL re-
738 sponse. Relations between the seaward-dipping pressure gradients (negative
739 $-dp/dx$) and δ_s are also not evident. This suggests that pressure gradient

740 forces are small and that the SFL growth is primarily driven by shear stresses
741 and bore turbulence. The processes governing SFL development are further
742 addressed in the Discussion (Section 6).

743 *4.3.2. Particle velocities*

744 The sand particle velocities in the sheet flow layer, u_p , were obtained
745 from the concentration measurements using the cross-correlation technique
746 by McLean et al. (2001), as explained in Section 2.4. The u_p measurements
747 were obtained for different concentration bins. The u_p measurements in the
748 lower SFL were somewhat noisy, likely due to the number of swash repeats
749 being too low for sufficient statistical convergence of the averaged cross-
750 correlations. Therefore, the analysis focuses here on the u_p measurements
751 obtained in the upper sheet flow layer corresponding to the concentration
752 range $C/C_{\text{bed}} = 0 - 0.2$. These velocities were derived from measurements
753 over approximately 60 T_R cycle repeats. Recall that particle velocities were
754 only measured by CCM⁺ tank 1, at $x = 1.28$ m. Figure 10b shows the
755 u_p measurements (circles), together with the ADV measurements of u at
756 $z - z_{\text{bed}} = 0.03$ m (solid line). Particle velocities were generally only measured
757 when the SFL is sufficiently developed, primarily during high landward (early
758 uprush) or seaward (mid backwash) free-stream velocity.

759 During the early uprush stages ($t/T_{\text{gr}} = 0.1 - 0.25$ and $1.05 - 1.15$) the
760 particle velocities in the SFL amount, on average, to 80 – 90% of the ADV
761 velocity. This suggests relatively high u up to close distance from the bed
762 and inside the SFL. Such approximately depth-uniform u at the leading edge
763 of the uprush would be consistent with previous observations and can be
764 explained by a limited time for boundary layer development at this lower

765 swash location (Kikkert et al., 2013) and by the turbulence that is produced
766 upon wave capture and that leads to strong vertical mixing of momentum
767 (Chen et al., 2016). On the other hand, u_p during the mid backwash stages
768 ($t/T_{\text{gr}} = 0.45 - 0.55$ and $1.55 - 1.75$) amounts to 50–60% of the ADV velocity.
769 These values are more consistent with SFL observations in tunnels (McLean
770 et al., 2001) and in wave flumes (Dohmen-Janssen and Hanes, 2002; van der
771 Zanden et al., 2017) and suggest a well developed shear layer, consistent with
772 other observations and numerical simulations of the quasi-steady backwash
773 (Sou and Yeh, 2011; Kikkert et al., 2013; Pintado-Patiño et al., 2015).

774 During the arrival of the third bore for event A (around $t/T_{\text{gr}} = 0.75$)
775 the ADV velocity decreases to nearly 0 m/s, but the u_p measurements in-
776 dicate that velocities in the SFL remain seaward directed and are of con-
777 siderable magnitude (-0.5 to -0.7 m/s). This reaffirms the occurrence of
778 multi-directional velocity over depth (see Section 4.1.3) and is consistent
779 with other measurements of simultaneous seaward near-bed flow and land-
780 ward free-stream flow in case of strong wave-backwash interactions (Pujara
781 et al., 2015b; Chen et al., 2016). The CCM⁺ measures u_p also during the fi-
782 nal backwash stages, when the ADV is exposed and the transport is confined
783 to thin swash lenses. During event A, u_p increases progressively in seaward
784 direction during the final, uninterrupted backwash ($t/T_{\text{gr}} = 0.80 - 1.00$).
785 Event B reveals a similar gradual increase ($t/T_{\text{gr}} = 1.55 - 1.70$) that is fol-
786 lowed by a gradual decrease during the very final stage of the backwash
787 ($t/T_{\text{gr}} = 1.70 - 1.95$) when the bed becomes exposed.

788 4.4. Sand transport rates

789 4.4.1. Calculations and assumptions

790 The intra-swash sand transport rates were estimated at the location of
791 CCM⁺ tank 1 ($x = 1.28$ m). Of specific interest are the temporal variation
792 of transport rates and the relative contributions of suspended and sheet flow
793 transport. These transport rates were not directly measured and their quan-
794 tification relies on assumptions on the vertical distributions of velocity and
795 concentration in the sheet flow and suspended layers, as explained in what
796 follows.

797 The depth-integrated sheet flow layer and suspended sand transport rates,
798 q_{sfl} and q_{susp} , are defined as:

$$q_{\text{sfl}} = \int_0^{\delta_s} u(\zeta)C(\zeta)d\zeta \quad (3)$$

799 and

$$q_{\text{susp}} = \int_{\delta_s}^h u(\zeta)C(\zeta)d\zeta = \gamma\hat{u}\hat{C}h \quad (4)$$

800 where $\zeta = z' - \delta_e(t)$ is the height relative to the bottom of the sheet
801 flow layer denoted by the erosion depth δ_e ; \hat{u} and \hat{C} are the depth-averaged
802 velocity and concentration, respectively; and γ is a shape coefficient.

803 To calculate q_{susp} , it is assumed that the depth-averaged velocity is rea-
804 sonably approximated by the ADV measurements at $z - z_{\text{bed}} = 0.03$ m, i.e.,
805 $\hat{u} = u(0.03 \text{ m})$. This assumption was justified in Section 4.1.3 on the basis
806 of velocity distributions observed over hydraulically smooth beds in other
807 swash studies. Note that for depth-uniform velocity, the shape coefficient
808 $\gamma = 1$.

809 Suspended sand concentrations in the swash tend to follow an exponential
 810 distribution (Masselink et al., 2005):

$$C(\zeta) = C_r \exp(-\zeta/l), \quad \delta_s \leq \zeta \leq h \quad (5)$$

811 where C_r is a reference concentration and l is a mixing length. Here, the
 812 exponential distribution is assumed to start at the top of the sheet flow layer.
 813 At this elevation ($\zeta = \delta_s$), $C = C_r = 0.12C_{\text{bed}}$. In order for Equation 5 to fit
 814 to the OBS-measured concentration C_{OBS} , it can be shown that the mixing
 815 length should equal:

$$l = \frac{\zeta_{\text{OBS}}}{\ln(C_r/C_{\text{OBS}})} \quad (6)$$

816 In which $\zeta_{\text{OBS}} = 0.03 + \delta_e$ is the height of the OBS relative to the bottom
 817 of the sheet flow layer. Depth-integration of Equation 5 from $\zeta = \delta_s$ to h
 818 yields the following expression for \hat{C} :

$$\hat{C} = \frac{C_{\text{OBS}}l}{h - \delta_s} [\exp(-\delta_s/l) - \exp(-h/l)] \quad (7)$$

819 Figure 10c shows C_{OBS} and \hat{C} , calculated through Equations 6 and 7.
 820 On average, $\hat{C} \approx 1.2C_{\text{OBS}}$.

821 The sand flux distribution in the sheet flow layer was calculated by mul-
 822 tiplying the concentration distribution obtained through Equation 2 with an
 823 empirical distribution for the particle velocity. The vertical profile of particle
 824 velocities in the sheet flow layer is generally considered to follow a power-form
 825 (e.g. Wilson, 1966; Sumer et al., 1996):

$$u_p(\zeta) = u_p(\delta_s) \left(\frac{\zeta}{\delta_s}\right)^n \quad (8)$$

826 where $u_p(\delta_s)$ is the particle velocity at the top of the sheet flow layer; n
 827 is an empirical shape factor. Values proposed for n are in the range of 0.5 to
 828 1 (Wilson, 1966; Sumer et al., 1996; Wang and Yu, 2007; Puleo et al., 2016,
 829 2017); $n = 0.75$ following Sumer et al. (1996) was adopted in the present
 830 study. The particle velocity at the top of the sheet flow layer was directly
 831 measured by the CCM⁺. Figure 11b shows the resulting u_p distribution.

832 An example of the flux distribution uC in the sheet flow layer is shown
 833 in Figure 11c. The flux increases strongly within the first few mm from
 834 the bed, reaches a maximum just below the pivot point, and then decreases
 835 gradually upward. This vertical distribution is consistent with direct mea-
 836 surements of the sheet flow flux in oscillatory flow tunnels (e.g. O’Donoghue
 837 and Wright, 2004b), in wave flumes under non-breaking and breaking waves
 838 (e.g. Schretlen, 2012; Fromant et al., 2018), and in dam-break swash (e.g.
 839 Wu et al., 2016).

840 The uncertainty associated with the quantification of the velocity and
 841 concentration profiles is estimated to be 30%, summing up to an uncertainty
 842 of 40–50% for q_{susp} and q_{sfl} . Although the uncertainty is considerable, it will
 843 be shown that the transport rates vary by up to a factor 10 in magnitude
 844 during a swash event. Hence, the results are considered sufficiently accurate
 845 for the analysis of the temporal variation of transport rates and of the relative
 846 importance of q_{susp} and q_{sfl} .

847 *4.4.2. Intra-swash time variation of sand transport rates*

848 The depth-integrated suspended and sheet flow transport rates are shown
849 in Figure 10e. For reference, the depth-averaged suspended sand concentra-
850 tion and the SFL thickness are shown in Figure 10c-d. Both parameters
851 follow a similar distribution in time.

852 Figure 10e shows that both transport modes are generally of similar mag-
853 nitude, consistent with previous observations in field (Horn and Mason, 1994)
854 and laboratory (Ruju et al., 2016; Puleo et al., 2016) swash. However, during
855 instants of intense sheet flow (around $t/T_{gr} = 0.75$ and $t/T_{gr} = 1.1$), q_{sfl} can
856 exceed q_{susp} by up to a factor five.

857 The uprush stages are characterized by relatively high landward-directed
858 q_{susp} and q_{sfl} . The sheet flow transport dominates during the uprush, with
859 q_{sfl} that exceeds q_{susp} by up to a factor two (event A) to five (event B). This
860 differs from previous estimates in the lab that suggested a dominance of q_{susp}
861 during the uprush (Ruju et al., 2016; Puleo et al., 2016). Such differences
862 may relate to strong variations of the bore impact on the bed depending
863 on wave conditions, cross-shore location, and sediment characteristics. For
864 instance, the study by Puleo et al. (2016) involved monochromatic waves,
865 hence the kinematics of the uprush bores may differ substantially from the
866 present study's, in which wave capture during the uprush occurs during both
867 events. In addition, the studies by Puleo et al. (2016) and Ruju et al. (2016)
868 both involved coarse sand whereas medium sand was used in the present
869 study. This difference in grain size leads to direct differences in the onset of
870 sheet flow, but also affects the hydrodynamic conditions in the swash, since
871 a coarser sand bed corresponds to steeper foreslopes and, consequently, more

872 reflective swash conditions.

873 During the early and mid backwash stages ($t/T_{\text{gr}} = 0.45 - 0.80$ and $1.45 -$
874 1.70) both transport modes are seaward-directed and q_{susp} tends to dominate.
875 An exception is formed during the strong wave-backwash interaction within
876 event A ($t/T_{\text{gr}} = 0.70 - 0.80$): during this stage, the increase in SFL thickness
877 in combination with the seaward-directed flow in the SFL leads to a large
878 seaward-directed peak in q_{sfl} , while the suspended sand transport reduces to
879 nearly 0 because of the low velocities higher in the water column. During
880 the late backwash stages ($t/T_{\text{gr}} = 0.80 - 1.05$ and $1.80 - 1.95$), q_{susp} could
881 not be measured but q_{sfl} is likely dominant due to the small water depths
882 (Masselink and Puleo, 2006).

883 5. Bed level changes and net transport rates

884 5.1. Intra-swash bed level changes

885 The intra-swash bed level changes already appeared in Section 4.3, but
886 are explored in more detail in the present section. Figure 12c shows the
887 intra-swash bed level changes measured by the two CCM⁺ tanks. The bed
888 level is here approximated by the sheet flow layer pivot point.

889 The bed at $x = -0.52$ m (red line) remains approximately steady during
890 event A. Apparently, cross-shore transport gradients are not steep enough
891 to promote significant bed level changes. During event B, the bed drops by
892 about 4 mm during the uprush ($t/T_{\text{gr}} = 1.0 - 1.1$) and it recovers during the
893 mid to late backwash ($t/T_{\text{gr}} = 1.7 - 2.0$). A stronger bed level variation is
894 revealed at $x = 1.28$ m (blue line). The first uprush event leads to a bed
895 erosion of about 8 mm ($t/T_{\text{gr}} = 0.1 - 0.2$, marked I). During the backwash,

896 the bed level accretes in two steps (during $t/T_{\text{gr}} = 0.5 - 0.6$ and $0.7 - 0.8$,
897 marked II and III). The total accretion by events II and III is approximately
898 16 mm. The uprush of event B ($t/T_{\text{gr}} = 1.05 - 1.15$, marked IV) leads to
899 a rapid erosion of approximately 7 mm at $x = 1.28$ m. This erosion rate is
900 similar to that observed for event A. During the remainder of event B the
901 bed at $x = 1.28$ m remains relatively stable with slight accretion during the
902 backwash.

903 Note that only a fraction of this eroded mass is stored locally in the water
904 column: estimates of the depth-integrated suspended load reach maximum
905 values up to 2 kg/m^2 , which corresponds to a bed level change of 1.3 mm.
906 Consequently, the bed level changes are not mainly due to changes in storage
907 as suspended load, but instead, to cross-shore gradients in q_{sfl} and q_{susp} .
908 Although both transport modes are likely to contribute, the transport in the
909 SFL is expected to be the most significant contributor to the bed level changes
910 because $q_{\text{sfl}}(t) > q_{\text{susp}}(t)$ and because the CCM⁺ measurements show that the
911 SFL dynamics in the lower swash alter rapidly with cross-shore distance.

912 Hence, the erosion events I and IV (Figure 12c) during the early uprush
913 stages are explained by an increasing landward transport rate at the swash
914 front as the bore propagates through the swash. The increasing suspended
915 sand concentration and SFL thickness at the swash front with cross-shore
916 distance (Sections 4.2 and 4.3) support this. The landward advected sand
917 is expected to be temporarily deposited in the mid/upper swash at the late
918 uprush phase, and then (partly) transported back in seaward direction during
919 the backwash as seaward velocities increase. Experimental evidence for this
920 explanation was given by Alsina et al. (2018) for similar swash conditions,

921 by means of simultaneous CCM⁺ measurements in the lower and mid swash
922 zones.

923 The stepwise increase in bed level at $x = 1.28$ m (accretion events II
924 and III) for swash event A relates to the altering of the backwash flow by
925 the third incident bore. The backwash induced by the first run-up of event
926 A has high seaward momentum in the mid swash and is at those locations
927 expected to mobilize considerable amounts of sediment. The backwash is
928 interrupted by the third incident bore ($t/T_{\text{gr}} = 0.52$), which enforces settling
929 out of suspended sediment grains and reduces the seaward-directed sheet flow
930 transport, hence promoting local accretion (accretion event II). This bore
931 subsequently leads to a strong wave-backwash interaction that promotes the
932 turbulent mobilization of sediment at $x \approx 1.8$ m, which is advected seaward
933 and deposited around the CCM⁺ location (accretion event III). The strong
934 bed level accretion (16 mm in total for events II and III) shows that the
935 transport associated with this backwash is highly cross-shore non-uniform,
936 with large changes in transport rates within $\mathcal{O}(0.1 \text{ to } 1 \text{ m})$ of cross-shore
937 distance.

938 The backwash during swash event B hardly induces bed level changes
939 in the lower swash. This is explained firstly by the lower momentum of this
940 backwash, hence leading to less mobilization of sand grains in the mid swash.
941 Secondly, the absence of any wave-swash interactions during the backwash
942 stage leads to a relatively uniform backwash flow in the lower swash and
943 transport gradients are expected to be low.

944 Magnitudes of bed level changes at $x = -0.52$ m (near transition inner
945 surf to lower swash zone) are considerably lower than at $x = 1.28$ m (near

946 transition lower to mid swash zone). This is consistent with observations of
947 suspended sand concentrations and SFL thickness, which also showed signif-
948 icantly less sediment mobilization at $x = -0.52$ m. The observed bed level
949 changes suggest that, at intra-swash time scale, a considerable amount of
950 sediment is transported within the swash zone, but that the sediment ex-
951 change between the swash and inner surf zones is weak in the present study.
952 Note that the present results complement the observations by Alsina et al.
953 (2018), who observed for similar wave conditions a strong intra-swash sedi-
954 ment exchange between the lower and mid to higher swash zones (the sedi-
955 ment exchange with the inner surf zone was not addressed in that study).

956 *5.2. Swash-averaged bed level changes*

957 The net (time-integrated) bed level changes induced by swash events A
958 and B were measured in the lower to upper swash by the conductivity-based
959 CCM⁺ sensors (at two cross-shore locations) and the acoustic wave gauges
960 (AWGs, seven locations). The AWG bed measurements were obtained dur-
961 ing intervals of bed exposure. Recall that a moving minimum with time
962 window equal to T_{gr} was applied to obtain the water depth h from the AWG
963 measurements (see Section 2.4). For the present analysis, the time window
964 was increased to $T_{\text{R}} = 2T_{\text{gr}}$. In this way, the overall bed evolution trend at
965 time scales $\geq T_{\text{R}}$ is filtered out, but net bed level changes by single events
966 A and B are preserved in the time series. This bed level detection technique
967 has been applied previously to laboratory swash measurements (Alsina et al.,
968 2012; Cáceres and Alsina, 2012).

969 To illustrate the technique, Figure 13 shows an example of the phase-
970 averaged AWG time series, where distinction is made between the identified

971 bed levels (brown circles) and water surface elevation (blue line). These bed
972 levels were obtained from the phase-averaged water depths as $h < 0.003$ m.
973 The time series in Figure 13 were vertically referenced with respect to the
974 mean bed level over both events A and B. The figure shows that the bed level
975 alters after each swash event, with net erosion induced by event A and net
976 accretion by event B at this location ($x = 3.5$ m). The phase-averaged bed
977 level measurements were used to calculate the net bed level change by events
978 A and B at each AWG cross-shore location. Subsequently, the bed level
979 change at time scales $> T_R$, obtained from the bed profile measurements,
980 was added.

981 Figure 14a shows the bed level changes by events A (blue) and B (red)
982 and the total bed level change by a full repeat cycle (i.e., events A and B
983 combined; black dashed line). The circles and squares mark the bed level
984 change measurements by AWG, which could be obtained for $x \geq 0.47$ m.
985 Further seaward, the bed was not fully exposed after each backwash. The
986 crosses represent the measurements by the CCM⁺ at two locations. The
987 good agreement between the collocated CCM⁺ and AWG measurements at
988 $x = 1.28$ m supports the adopted approach. The dashed blue and red lines
989 represent a cubic interpolation of the bed level measurements.

990 The results show a strong cross-shore variation in net bed level change.
991 Swash event A leads to net erosion in the mid swash and accretion in the
992 lower and upper swash zones. Patterns for event B are nearly the exact
993 opposite of event A. The net total bed level change (black dashed line) is
994 the small difference between the bed change by both events. The latter
995 implies that the bed profile is in a “dynamic quasi-equilibrium”, where each

996 single event induces significant morphodynamic change, but where the rate
997 of change over multiple events is minor. Event A induces net accretion in
998 the upper swash, associated with the high run-up of this event that stores
999 sediment at the beach. The bed level in the upper swash decreases slightly
1000 during event B, even though the maximum run-up does not reach further
1001 than $x \approx 6$ m. The decrease in bed level is either due to seaward transport
1002 in very thin water films, or due to compaction of the bed as the beach drains.
1003 Largest bed level changes are observed in the lower swash, likely due to the
1004 occurrence of wave-swash interactions (further addressed in next section).
1005 These results are consistent with field measurements by Blenkinsopp et al.
1006 (2011), who also observed largest bed level changes in the lower swash.

1007 *5.3. Net sand transport rate by single and multiple swash events*

1008 The net bed level changes can be used to quantify the net sand transport
1009 over both events A and B. This was done by solving the sediment mass
1010 balance (Equation 1), starting from the landward boundary, using the cubic
1011 interpolated bed changes (dashed line in Figure 14a). The obtained net total
1012 sand transport rates q_{tot} for the two events are shown in Figure 14b (solid
1013 lines).

1014 In the lower swash near the run-down ($x < 1.1$ m), event A induces
1015 net landward and event B induces net seaward transport. This may be
1016 explained in terms of velocity variations, as event A is at these locations
1017 characterized by relatively high uprush velocities and B by relatively high
1018 backwash velocities. Slightly landward ($x > 1.1$ m), near the transition from
1019 lower to mid swash, q_{tot} changes sign and the cross-shore transport gradients
1020 dq_{tot}/dx reach a maximum. This likely relates to the occurrence of various

1021 types of wave-swash interactions that have a large effect on the local flow
1022 conditions. At the location of CCM⁺ tank 1 ($x = 1.28$ m) the net transport is
1023 seaward for event A and landward for event B. This is qualitatively consistent
1024 with the observations of $q_{\text{susp}}(t)$ and $q_{\text{sfl}}(t)$ (Section 4.4) that showed high
1025 seaward transport during the backwash of event A (associated with the strong
1026 wave-backwash interaction) and high landward transport during the uprush
1027 of event B (associated with the merged bore propagating over the exposed
1028 bed). Maximum seaward q_{tot} for event A occurs in the mid swash, landward
1029 from the location of the strong wave-backwash interaction for this event
1030 ($x = 1.8$ m). This implies that this wave-backwash interaction, although
1031 mobilizing significant amounts of sediment, does not enhance the net seaward
1032 transport - on the contrary, because it halts the backwash, it reduces the
1033 seaward transport of sediment in the lower swash.

1034 In the mid swash, event A generates net seaward transport. This likely
1035 relates to the relatively long, uninterrupted backwash for this event that pro-
1036 duces high seaward velocity. Maximum net seaward transport is observed at
1037 $x = 2.1$ m, landward from the strong wave-backwash interaction. The trans-
1038 port for event B is landward in the mid swash which may relate to the rela-
1039 tively high landward transport during the uprush (see also OBS and CCM⁺
1040 measurements) due to wave capture in the lower swash and the onshore ad-
1041 vection of sediment as suspended and sheet load. In the upper swash, event
1042 A leads to net onshore transport as the large run-up advects sediment land-
1043 ward and stores it at the berm. The net seaward transport for event B may
1044 be physical and contained in very thin swash lenses, or an artifact of the
1045 compacting bed as the upper swash is drained.

1046 Several studies have suggested that swash morphodynamics are driven
1047 by the combination of (1) the sediment that is mobilized within the swash
1048 zone and redistributed across the swash and (2) the sediment that is “pre-
1049 mobilized” in the inner surf zone and that is imported/exported at the sea-
1050 ward boundary of the swash (Jackson et al., 2004; Pritchard and Hogg, 2005;
1051 Alsina et al., 2009). The importance of the pre-mobilized sand in the present
1052 study can be studied by comparing the transport rates near the run-down
1053 location with those observed along the swash zone. Figure 14b shows that
1054 at $x = -0.5$ m, $q_{\text{tot}} = +0.17$ kg/ms for event A and $q_{\text{tot}} = -0.29$ kg/ms
1055 for event B. Integrated over a swash event, these values correspond to a net
1056 sediment import from surf to swash of 2.5 kg/m for event A and a net export
1057 of 4.3 kg/m for event B. Transport rates increase by up to a factor four in
1058 magnitude between the run-down location to the mid swash zone. This im-
1059 plies that the net bed level changes by events A and B are largely due to a
1060 cross-shore redistribution of sediment within the swash, with a smaller (but
1061 not negligible) contribution of the sand exchanged with the inner surf zone.

1062 Finally, the transport rates averaged over both events, i.e., at the repeat
1063 frequency, is analysed (Figure 14b, dashed black line). Similar to the bed level
1064 changes, the alternating swash events A and B generate q_{tot} that is at each
1065 cross-shore location of similar magnitude but opposite sign. Consequently,
1066 the net transport over the repeat cycle at each location is the small difference
1067 between large landward or seaward transport rates by a single event. The
1068 transport over the repeat cycle is generally seaward directed, consistent with
1069 a gradual erosion of the beach. Averaged over both events, the transport
1070 rate at the surf-swash boundary is high relative to the transport rates in the

1071 mid swash. This implies that at longer time scales, the sediment exchange
1072 between surf and swash zone becomes increasingly significant for swash zone
1073 morphodynamics.

1074 The results show that the significance of the transport across the surf-
1075 swash boundary for the overall swash zone morphodynamics depends strongly
1076 on the time scale of interest (intra-swash, swash-averaged over single events,
1077 or averaged over multiple events). Section 6.4 reflects further on this issue.

1078 **6. Discussion**

1079 *6.1. Experiments*

1080 Due to the non-uniformity of the flow and sand transport in the swash,
1081 transport processes and net transport rates can vary significantly within short
1082 cross-shore distance, especially in the lower swash region where various types
1083 of wave-swash interactions occur. Measurements in the present study cover
1084 the swash zone with relatively high spatial coverage compared to previous
1085 studies. Nevertheless, the flow non-uniformity and the advective cross-shore
1086 influx as suspended and sheet load from adjacent locations complicates the
1087 interpretation of sand transport physics in the swash, which are not at all
1088 governed by purely local hydrodynamic forcing. Consequently, the interpre-
1089 tation of the governing processes based on few local measurements proves
1090 to be difficult and subject to conjecturing. Future studies may therefore
1091 be aimed at obtaining an even higher spatial coverage of flow velocity, sus-
1092 pended sand concentration, and sheet flow measurements across the inner
1093 surf to upper swash zone. In terms of net bed level measurements and trans-
1094 port rates by AWGs, the limited spatial coverage of measurements ($\Delta x \approx 1$

1095 m) required a spatial interpolation that inherently leads to smoothening of
1096 the transport rates. This could not be overcome with the instruments avail-
1097 able for the present study. However, techniques to measure the exposed bed
1098 level with high spatial coverage and vertical accuracy are available, e.g. LI-
1099 DAR (Blenkinsopp et al., 2010; Almeida et al., 2015) or stereoscopic imaging
1100 (Astruc et al., 2012), for future studies.

1101 *6.2. Insights for numerical modeling of sheet flow transport in the swash*

1102 Consistent with previous swash observations (e.g., Masselink et al., 2005),
1103 sheet flow occurred especially during the early uprush and mid/late backwash
1104 stages. The sheet flow layer (SFL) reaches thicknesses up to $\delta_s = 30$ mm,
1105 or $\delta_s/D_{50} = 120$. Although such thicknesses are similar to previous observa-
1106 tions in the swash (e.g., Lanckriet and Puleo, 2015; van der Zanden et al.,
1107 2015; Alsina et al., 2018), they are relatively high (given the measured ve-
1108 locity) in comparison to previous medium-sand sheet flow observations, e.g.
1109 in oscillatory flow tunnels (Ribberink and Al-Salem, 1995; Hassan and Rib-
1110 berink, 2005) and under non-breaking waves (Dohmen-Janssen and Hanes,
1111 2002; Schretlen, 2012; van der Zanden et al., 2017). This reaffirms that the
1112 relation between free-stream velocity and SFL dynamics in the swash differs
1113 from that for non-breaking waves, and that additional processes contribute
1114 to SFL growth (see e.g. Lanckriet and Puleo, 2015). The present measure-
1115 ments do not reveal any evidence for cross-shore pressure gradient effects on
1116 SFL growth. Hence, the results do not reaffirm previous studies that sug-
1117 gested significant effects of the cross-shore pressure gradient on SFL thick-
1118 ness (Lanckriet and Puleo, 2015), but rather support the results by (Othman
1119 et al., 2014) who found minor significance for pressure gradient effects on the

1120 transport of fine to medium sand in the swash. The large SFL thickness dur-
1121 ing the uprush may relate to bore turbulence (Lanckriet and Puleo, 2015)
1122 and/or a high bed shear stress at the leading edge of the swash due to flow
1123 convergence and limited time for boundary layer development (Barnes et al.,
1124 2009; Kikkert et al., 2012). In addition, the SFL measurements reaffirm the
1125 significance of cross-shore sheet load advection and wave-swash interactions,
1126 consistent with earlier observations for narrow-banded erosive swash events
1127 (van der Zanden et al., 2015; Alsina et al., 2018).

1128 The significance of sediment advection implies that numerical models for
1129 sand transport in the swash should best use advection-diffusion type models,
1130 instead of the more common “local” empirical bedload transport models, to
1131 resolve the transport in the sheet flow layer. Although several studies have
1132 developed 1DV advection-diffusion approaches to simulate sheet flow dynam-
1133 ics in tunnels and under non-breaking waves (Li and Davies, 2001; Holmedal
1134 et al., 2004; Kranenburg et al., 2013; Caliskan and Fuhrman, 2017), to the au-
1135 thors knowledge, advection-diffusion models have never been applied to the
1136 (2DV) sheet flow transport in the swash. The results in the present study
1137 show remarkable similarity in terms of the spatial and temporal variation
1138 of suspended sand concentration and sheet flow layer thickness, which sug-
1139 gests that suspension and sheet flow are governed by similar hydrodynamic
1140 forcing processes. This implies that a total load approach for the combined
1141 sheet load and suspended load may also be well suitable for the swash. Two-
1142 phase approaches (e.g., Bakhtyar et al., 2010) can also be used to simulate
1143 the advection-diffusion of sand as sheet flow, but are generally much more
1144 computationally expensive.

1145 *6.3. Effects of wave-swash interactions on sand transport*

1146 Wave-swash interactions have a strong effect on sand transport processes
1147 in the present study, consistent with earlier observations that address the
1148 roles of wave-swash interactions on sand suspension (Hughes and Moseley,
1149 2007; Cáceres and Alsina, 2012) and on sheet flow dynamics (Alsina et al.,
1150 2018). The key swash interactions in the present study are the wave capture
1151 for both events and the strong wave-backwash interaction for event A. The
1152 cross-shore location of wave capture has a large effect on uprush transport,
1153 as it determines whether a swash front propagates over a dry bed (leading
1154 to high bed shear stress) or whether it propagates over a preceding, smaller
1155 bore (which reduces the bed shear stress) (Barnes et al., 2009; Baldock et al.,
1156 2014). Wave capture also leads to high turbulence production (Chen et al.,
1157 2016) and high turbulence levels are expected landward of the capture point.
1158 The higher mobilization of sediment as sheet load and suspended load by
1159 the uprush of event B, which had the wave capture point located further
1160 seaward than event A, likely connects to these hydrodynamic processes. The
1161 strong wave-backwash interaction for event A is also effective in terms of
1162 mobilizing sediment, increasing SFL thickness as well as suspended sand
1163 concentrations. This is consistent with previous suspension measurements
1164 (Hughes and Moseley, 2007; Cáceres and Alsina, 2012; Alsina et al., 2018)
1165 and can be explained by the high turbulence levels generated by velocity
1166 shearing as the backwash and incident bore collide and a stationary bore is
1167 formed (Chen et al., 2016).

1168 The wave-swash interactions also affect the net transport and, conse-
1169 quently, bed level changes in the swash. It is likely that the location of the

1170 cross-shore maximum in uprush transport relates to the location of wave
1171 capture during the uprush: landward from this location, the merged, highly
1172 turbulent bore propagates over a dry bed and is expected to induce high bed
1173 shear stresses and sediment mobilization. As the bore propagates landward
1174 throughout the swash, bed shear stresses and turbulence levels are expected
1175 to reduce as the turbulent energy dissipates and the bore is retarded by
1176 gravity. One may therefore expect maximum landward transport shortly
1177 landward from the wave capture location. This explanation is supported by
1178 the differences in uprush transport for events A and B. Strong wave-backwash
1179 interactions interrupt the backwash velocity and reduce the seaward trans-
1180 port. The weak wave-backwash interaction appears to have little effect on
1181 sediment transport processes and rates. Note that the present study only
1182 covers a small number of wave-swash interactions and further study is re-
1183 quired to verify the generality of these results.

1184 *6.4. Net morphodynamic change*

1185 The results in Section 4 reveal significant mobilization and transport of
1186 sediment as sheet flow and suspended load in the lower to mid swash zone.
1187 This contrasts with the inner surf-lower swash boundary, where measured
1188 sediment concentrations and sheet flow layer thicknesses are low. This possi-
1189 bly reflects much lower bed shear stresses in the inner surf zone compared to
1190 the lower swash (see e.g., Barnes et al., 2009). Moreover, the measurements
1191 indicate a considerable increase in net transport rates by single events in
1192 the lower swash zone compared to the surf-swash boundary. These results
1193 imply that most of the sand transported in the swash zone was mobilized
1194 within the swash zone, and that the contribution of pre-suspended sediment,

1195 mobilized in the inner surf zone and then imported into the swash zone,
1196 was considerably smaller. This contrasts with field observations (Jackson
1197 et al., 2004; Hughes and Moseley, 2007) and numerical studies (Pritchard
1198 and Hogg, 2005; Alsina et al., 2009) that found significant contributions of
1199 pre-suspended sediment to the total transport in the swash. Differences
1200 with the field observations may relate to variations in the determining of
1201 the moving surf-swash boundary. The differences with numerical studies
1202 may partly relate to the significant effects of swash-specific processes, e.g.,
1203 the bore run-up over a dry bed and the wave-backwash interactions, that
1204 were not (fully) incorporated in the numerical model formulations for sed-
1205 iment transport. Note that although the sand exchange between the surf
1206 and swash is relatively small (compared to transport rates within the swash
1207 zone) at intra-swash time scale, the results show that its significance to swash
1208 zone morphologic change increases progressively with time scale (i.e., from
1209 intra-swash, to event-averaged, to averaged over multiple events). The rel-
1210 ative significance of the sediment advection across the surf-swash boundary
1211 compared to sediment that is mobilized within the swash zone is summarized
1212 for different time scales in Table 2.

1213 The measurements further show a large variability between swash events,
1214 with opposite net transport rates and bed level changes for events A and
1215 B. The net transport and morphodynamic change over the two events com-
1216 bined is the small difference between transport and changes in opposite di-
1217 rections. At intra-swash time scale (Section 4.3), transport rates and bed
1218 level changes are even greater. The decrease in the transport rate and mor-
1219 phodynamic change of interest with increasing time scales is summarized

1220 for the present study in Table 2. These results are in line with field ob-
1221 servations that showed that various single erosive and accretive events can
1222 nearly balance in terms of net transport, leading to small morphodynamic
1223 rates of change at longer time scales (Masselink et al., 2009; Blenkinsopp
1224 et al., 2011). Hence, the present experiment reaffirms the need for methods
1225 to upscale the short-term processes to longer-term beach evolution, which is
1226 considered one of the main challenges for research on swash morphodynamics
1227 (Chardón-Maldonado et al., 2016).

1228 **7. Conclusions**

1229 Measurements are presented of a large-scale wave flume experiment that
1230 involved two alternating swash events A and B, formed by two bichromatic
1231 wave groups with a phase modulation.

1232 Event A is characterized by a strong uprush with high velocity and run-
1233 up length that contributes to building of the berm in the upper swash. Its
1234 backwash reaches high seaward-directed velocity and erodes the mid swash,
1235 but the interruption of the backwash flow by a third incident bore induces
1236 deposition of sediment in the lower swash.

1237 Event B is characterized by two uprush and backwash events, with gen-
1238 erally lower velocities and weaker wave-swash interactions than for event A.
1239 The primary uprush of event B is formed by two incident bores that merge
1240 close to the surf-swash boundary. The uprush propagates over an exposed
1241 bed in the lower swash, leading to net erosion at these locations, and ad-
1242 vects the eroded sediment landward to the mid swash, leading to local net
1243 accretion.

1244 Together, the two alternating swash events produce a dynamic equilib-
1245 rium of the bed, where bed level changes induced by single events are signif-
1246 icant (up to 8 mm) but the net bed change integrated over the two events
1247 is relatively small (up to 1 mm). These net changes become nevertheless
1248 significant when integrated over time scales of minutes to hours, and it ex-
1249 plains the gradual erosion of the swash zone as observed with bed profiler
1250 measurements in the present experiment.

1251 The observations of sediment transport processes further lead to the fol-
1252 lowing specific conclusions:

- 1253 • The mobilization of sediment as suspended and sheet load increases
1254 significantly landward from the wave capture point (where a large inci-
1255 dent bore overtakes a preceding, smaller, incident bore). Consequently,
1256 the location of wave capture has a large effect on sand resuspension and
1257 transport during the uprush. No clear relation is found between cross-
1258 shore pressure gradients and sheet flow layer growth.
- 1259 • Sheet flow and suspended load transport rates in the lower swash are
1260 generally of the same order of magnitude, but the sheet flow transport
1261 exceeds the suspended transport by a factor four during the early up-
1262 rush stage. Sheet flow is further expected to dominate during the final
1263 backwash stage.
- 1264 • Instantaneous bed level changes ($\mathcal{O}(\text{cm/s})$) are highest in the lower
1265 swash zone and occur especially during the early uprush and during
1266 instants of strong wave-swash interactions during the backwash. This
1267 relates to the strongly non-uniform flow at these moments. For the

1268 same reason, also the net bed level changes (integrated over single swash
1269 events) are maximum in the lower swash zone.

1270 • Sand transport rates and bed level changes at intra-swash time scales
1271 can be orders of magnitude greater than the net transport rates and
1272 bed level change integrated over both events.

1273 • Also the relative importance of the sand exchange between surf and
1274 swash zone varies with time scale. At intra-swash time scales and in-
1275 tegrated over single swash events, the advection across the surf-swash
1276 boundary is of minor significance and bed level changes in the swash
1277 are primarily explained by sand redistribution within the swash. How-
1278 ever, at time scales over multiple events or over 60-min experimental
1279 runs, the net sand exchange between the surf and swash zone becomes
1280 increasingly important.

1281 **Acknowledgments**

1282 The experiments described in this publication were supported by the
1283 European Communitys Horizon 2020 Programme through the grant to the
1284 budget of the Integrated Infrastructure Initiative HYDRALAB+, Contract
1285 no. 654110, and was conducted as part of the transnational access project
1286 RESIST. JvdZ and JJvdW gratefully acknowledge funding by NWO-TTW
1287 (contract no. 16130) and SE gratefully acknowledges funding from the De-
1288 partment of Civil and Environmental Engineering, Imperial College London.
1289 We thank fellow RESIST researchers and the CIEMLAB staff (Oscar Galego,
1290 Andrea Marzeddu, and Joaquim Sospedra) for their contributions to the ex-

1291 periments. Finally, we are grateful to the two reviewers for their constructive
1292 feedback on the initial submitted manuscript.

1293 **References**

1294 Aagaard, T., Hughes, M. G., 2006. Sediment suspension and turbulence in
1295 the swash zone of dissipative beaches. *Marine Geology* 228 (1-4), 117–135.

1296 Almeida, L. P., Masselink, G., Russell, P. E., Davidson, M. A., 2015. Obser-
1297 vations of gravel beach dynamics during high energy wave conditions using
1298 a laser scanner. *Geomorphology* 228, 15–27.

1299 Alsina, J. M., Cáceres, I., 2011. Sediment suspension events in the inner
1300 surf and swash zone. measurements in large-scale and high-energy wave
1301 conditions. *Coastal Engineering* 58 (8), 657–670.

1302 Alsina, J. M., Cáceres, I., Brocchini, M., Baldock, T. E., 2012. An exper-
1303 imental study on sediment transport and bed evolution under different
1304 swash zone morphological conditions. *Coastal Engineering* 68, 31–43.

1305 Alsina, J. M., Falchetti, S., Baldock, T. E., 2009. Measurements and mod-
1306 elling of the advection of suspended sediment in the swash zone by solitary
1307 waves. *Coastal Engineering* 56 (5-6), 621–631.

1308 Alsina, J. M., Padilla, E. M., Cáceres, I., 2016. Sediment transport and beach
1309 profile evolution induced by bi-chromatic wave groups with different group
1310 periods. *Coastal Engineering* 114, 325–340.

- 1311 Alsina, J. M., van der Zanden, J., Cáceres, I., Ribberink, J. S., 2018. The in-
1312 fluence of wave groups and wave-swash interactions on sediment transport
1313 and bed evolution in the swash zone. *Coastal Engineering* 140, 23–42.
- 1314 Astruc, D., Cazin, S., Cid, E., Eiff, O., Lacaze, L., Robin, P., Toub Blanc, F.,
1315 Cáceres, I., 2012. A stereoscopic method for rapid monitoring of the spatio-
1316 temporal evolution of the sand-bed elevation in the swash zone. *Coastal*
1317 *Engineering* 60, 11–20.
- 1318 Bakhtyar, R., Barry, D. A., Yeganeh-Bakhtiary, A., Li, L., Parlange, J. Y.,
1319 Sander, G. C., 2010. Numerical simulation of two-phase flow for sediment
1320 transport in the inner-surf and swash zones. *Advances in Water Resources*
1321 33 (3), 277–290.
- 1322 Baldock, T. E., 2006. Long wave generation by the shoaling and breaking
1323 of transient wave groups on a beach. *Proceedings of the Royal Society*
1324 *a-Mathematical Physical and Engineering Sciences* 462 (2070), 1853–1876.
- 1325 Baldock, T. E., 2012. Dissipation of incident forced long waves in the surf
1326 zone implications for the concept of bound wave release at short wave break-
1327 ing. *Coastal Engineering* 60, 276–285.
- 1328 Baldock, T. E., Alsina, J. M., Cáceres, I., Vicinanza, D., Contestabile, P.,
1329 Power, H., Sanchez-Arcilla, A., 2011. Large-scale experiments on beach
1330 profile evolution and surf and swash zone sediment transport induced by
1331 long waves, wave groups and random waves. *Coastal Engineering* 58 (2),
1332 214–227.

- 1333 Baldock, T. E., Birrien, F., Atkinson, A., Shimamoto, T., Wu, S., Callaghan,
1334 D. P., Nielsen, P., 2017. Morphological hysteresis in the evolution of beach
1335 profiles under sequences of wave climates - part 1; observations. *Coastal*
1336 *Engineering* 128, 92–105.
- 1337 Baldock, T. E., Grayson, R., Torr, B., Power, H. E., 2014. Flow convergence
1338 at the tip and edges of a viscous swash front experimental and analytical
1339 modeling. *Coastal Engineering* 88, 123–130.
- 1340 Baldock, T. E., Hughes, M. G., 2006. Field observations of instantaneous wa-
1341 ter slopes and horizontal pressure gradients in the swash-zone. *Continental*
1342 *Shelf Research* 26 (5), 574–588.
- 1343 Baldock, T. E., Huntley, D. A., Bird, P. A. D., O’Hare, T., Bullock, G. N.,
1344 2000. Breakpoint generated surf beat induced by bichromatic wave groups.
1345 *Coastal Engineering* 39 (2-4), 213–242.
- 1346 Barnes, M. P., Baldock, T. E., 2010. A lagrangian model for boundary layer
1347 growth and bed shear stress in the swash zone. *Coastal Engineering* 57 (4),
1348 385–396.
- 1349 Barnes, M. P., O’Donoghue, T., Alsina, J. M., Baldock, T. E., 2009. Direct
1350 bed shear stress measurements in bore-driven swash. *Coastal Engineering*
1351 56 (8), 853–867.
- 1352 Battjes, J. A., Bakkenes, H. J., Janssen, T. T., van Dongeren, A. R., 2004.
1353 Shoaling of subharmonic gravity waves. *Journal of Geophysical Research*
1354 109 (C2).

- 1355 Blenkinsopp, C., Mole, M. E., Turner, I. L., Peirson, W. L., 2010. Measure-
1356 ments of the time-varying profile across the swash zone using an industrial
1357 lidar. *Coastal Engineering*.
- 1358 Blenkinsopp, C. E., Turner, I. L., Masselink, G., Russell, P. E., 2011. Swash
1359 zone sediment fluxes: Field observations. *Coastal Engineering* 58 (1), 28–
1360 44.
- 1361 Bonneton, P., Lannes, D., Martins, K., Michallet, H., 2018. A nonlinear
1362 weakly dispersive method for recovering the elevation of irrotational surface
1363 waves from pressure measurements. *Coastal Engineering* 138, 1–8.
- 1364 Briganti, R., Dodd, N., Pokrajac, D., O’Donoghue, T., 2011. Non linear
1365 shallow water modelling of bore-driven swash: Description of the bottom
1366 boundary layer. *Coastal Engineering* 58 (6), 463–477.
- 1367 Briganti, R., Torres-Freyermuth, A., Baldock, T. E., Brocchini, M., Dodd,
1368 N., Hsu, T.-J., Jiang, Z., Kim, Y., Pintado-Patiño, J. C., Postacchini, M.,
1369 2016. Advances in numerical modelling of swash zone dynamics. *Coastal*
1370 *Engineering* 115, 26–41.
- 1371 Brocchini, M., Baldock, T. E., 2008. Recent advances in modeling swash zone
1372 dynamics: Influence of surf-swash interaction on nearshore hydrodynamics
1373 and morphodynamics. *Reviews of Geophysics* 46 (3).
- 1374 Brocchini, M., Peregrine, D. H., 1996. Integral flow properties of the swash
1375 zone and averaging. *Journal of Fluid Mechanics* 317, 241–273.
- 1376 Butt, T., Russell, P., 1999. Suspended sediment transport mechanisms in
1377 high-energy swash. *Marine Geology* 161 (2-4), 361–375.

- 1378 Cáceres, I., Alsina, J. M., 2012. A detailed, event-by-event analysis of sus-
1379 pended sediment concentration in the swash zone. *Continental Shelf Re-*
1380 *search* 41, 61–76.
- 1381 Cáceres, I., Alsina, J. M., 2016. Suspended sediment transport and beach dy-
1382 namics induced by monochromatic conditions, long waves and wave groups.
1383 *Coastal Engineering* 108, 36–55.
- 1384 Caliskan, U., Fuhrman, D. R., 2017. Rans-based simulation of wave-induced
1385 sheet-flow transport of graded sediments. *Coastal Engineering* 121, 90–102.
- 1386 Chardón-Maldonado, P., Pintado-Patiño, J. C., Puleo, J. A., 2016. Advances
1387 in swash-zone research: Small-scale hydrodynamic and sediment transport
1388 processes. *Coastal Engineering* 115, 8–25.
- 1389 Chen, B.-T., Kikkert, G. A., Pokrajac, D., Dai, H.-J., 2016. Experimental
1390 study of bore-driven swash-swash interactions on an impermeable rough
1391 slope. *Coastal Engineering* 108, 10–24.
- 1392 Dohmen-Janssen, C. M., Hanes, D., 2002. Sheet flow dynamics under
1393 monochromatic nonbreaking waves. *Journal of Geophysical Research*
1394 107 (C10).
- 1395 Dohmen-Janssen, C. M., Hanes, D. M., 2005. Sheet flow and suspended
1396 sediment due to wave groups in a large wave flume. *Continental Shelf*
1397 *Research* 25 (3), 333–347.
- 1398 Dohmen-Janssen, C. M., Hassan, W. N., Ribberink, J. S., 2001. Mobile-bed
1399 effects in oscillatory sheet flow. *Journal of Geophysical Research-Oceans*
1400 106 (C11), 27103–27115.

- 1401 Downing, J. P., Beach, R. A., 1989. Laboratory apparatus for calibrating
1402 optical suspended solids sensors. *Marine Geology* 86 (2-3), 243–249.
- 1403 Eichertopf, S., van der Zanden, J., Cáceres, I., Baldock, T., Alsina, J. M.,
1404 2019. Influence of storm sequencing on breaker bar and shoreline evolution
1405 in large-scale experiments. *Coastal Engineering* , in preparation.
- 1406 Fromant, G., Hurther, D., van der Zanden, J., van der A, D. A., Cáceres,
1407 I., ODonoghue, T., Ribberink, J. S., 2018. Wave boundary layer hydrody-
1408 namics and sheet flow properties under large-scale plunging-type breaking
1409 waves. *Journal of Geophysical Research: Oceans*.
- 1410 Hassan, W. N., Ribberink, J. S., 2005. Transport processes of uniform and
1411 mixed sands in oscillatory sheet flow. *Coastal Engineering* 52 (9), 745–770.
- 1412 Hibberd, S., Peregrine, D. H., 1979. Surf and run-up on a beach - uniform
1413 bore. *Journal of Fluid Mechanics* 95 (Nov), 323–345.
- 1414 Higuera, P., Liu, P. L. F., Lin, C., Wong, W. Y., Kao, M. J., 2018.
1415 Laboratory-scale swash flows generated by a non-breaking solitary wave
1416 on a steep slope. *Journal of Fluid Mechanics* 847, 186–227.
- 1417 Holmedal, L. E., Myrhaug, D., Eidsvik, K. J., 2004. Sediment suspension un-
1418 der sheet flow conditions beneath random waves plus current. *Continental*
1419 *Shelf Research* 24 (17), 2065–2091.
- 1420 Horn, D. P., Mason, T., 1994. Swash zone sediment transport modes. *Marine*
1421 *Geology* 120 (3-4), 309–325.

- 1422 Hughes, M., 1995. Friction factor for wave uprush. *Journal of Coastal Re-*
1423 *search* 11 (4), 1069–1096.
- 1424 Hughes, M. G., Moseley, A. S., 2007. Hydrokinematic regions within the
1425 swash zone. *Continental Shelf Research* 27 (15), 2000–2013.
- 1426 Incelli, G., Dodd, N., Blenkinsopp, C. E., Zhu, F., Briganti, R., 2016. Mor-
1427 phodynamical modelling of field-scale swash events. *Coastal Engineering*
1428 115, 42–57.
- 1429 Jackson, N. L., Masselink, G., Nordstrom, K. F., 2004. The role of bore
1430 collapse and local shear stresses on the spatial distribution of sediment
1431 load in the uprush of an intermediate-state beach. *Marine Geology* 203 (1-
1432 2), 109–118.
- 1433 Janssen, T. T., Battjes, J. A., van Dongeren, A. R., 2003. Long waves in-
1434 duced by short-wave groups over a sloping bottom. *Journal of Geophysical*
1435 *Research-Oceans* 108 (C8), 1–14.
- 1436 Jonsson, I. G., 1980. A new approach to oscillatory rough turbulent boundary
1437 layers. *Ocean Engineering* 7 (1), 109–152.
- 1438 Kikkert, G. A., O’Donoghue, T., Pokrajac, D., Dodd, N., 2012. Experimental
1439 study of bore-driven swash hydrodynamics on impermeable rough slopes.
1440 *Coastal Engineering* 60, 149–166.
- 1441 Kikkert, G. A., Pokrajac, D., O’Donoghue, T., Steenhauer, K., 2013. Exper-
1442 imental study of bore-driven swash hydrodynamics on permeable rough
1443 slopes. *Coastal Engineering* 79, 42–56.

- 1444 Kim, Y., Zhou, Z., Hsu, T.-J., Puleo, J. A., 2017. Large eddy simulation of
1445 dam-break-driven swash on a rough-planar beach. *Journal of Geophysical*
1446 *Research: Oceans* 122 (2), 1274–1296.
- 1447 Kobayashi, N., Johnson, B. D., 2001. Sand suspension, storage, advection,
1448 and settling in surf and swash zones. *Journal of Geophysical Research*
1449 106 (C5), 9363–9376.
- 1450 Kranenburg, W. M., Ribberink, J. S., Schretlen, J. J. L. M., Uittenbogaard,
1451 R. E., 2013. Sand transport beneath waves: The role of progressive wave
1452 streaming and other free surface effects. *Journal of Geophysical Research:*
1453 *Earth Surface* 118 (1), 122–139.
- 1454 Lanckriet, T., Puleo, J. A., 2015. A semianalytical model for sheet flow
1455 layer thickness with application to the swash zone. *Journal of Geophysical*
1456 *Research-Oceans* 120 (2), 1333–1352.
- 1457 Lanckriet, T., Puleo, J. A., Masselink, G., Turner, I. L., Conley, D., Blenk-
1458 insopp, C., Russell, P., 2014. Comprehensive field study of swash-zone
1459 processes. ii: Sheet flow sediment concentrations during quasi-steady back-
1460 wash. *Journal of Waterway, Port, Coastal, and Ocean Engineering* 140 (1),
1461 29–42.
- 1462 Lara, J. L., Ruju, A., Losada, I. J., 2011. Reynolds averaged navier-stokes
1463 modelling of long waves induced by a transient wave group on a beach. *Pro-*
1464 *ceedings of the Royal Society A: Mathematical, Physical and Engineering*
1465 *Sciences* 467 (2129), 1215–1242.

- 1466 Li, Z., Davies, A. G., 2001. Turbulence closure modelling of sediment trans-
1467 port beneath large waves. *Continental Shelf Research* 21 (3), 243–262.
- 1468 Longuet-Higgins, M. S., Stewart, R. W., 1962. Radiation stress and mass
1469 transport in gravity waves, with application to surf beats. *Journal of Fluid*
1470 *Mechanics* 13 (04), 481.
- 1471 Masselink, G., Evans, D., Hughes, M. G., Russell, P., 2005. Suspended sedi-
1472 ment transport in the swash zone of a dissipative beach. *Marine Geology*
1473 216 (3), 169–189.
- 1474 Masselink, G., Hughes, M., 1998. Field investigation of sediment transport
1475 in the swash zone. *Continental Shelf Research* 18 (10), 1179–1199.
- 1476 Masselink, G., Puleo, J. A., 2006. Swash-zone morphodynamics. *Continental*
1477 *Shelf Research* 26 (5), 661–680.
- 1478 Masselink, G., Russell, P., Turner, I., Blenkinsopp, C., 2009. Net sediment
1479 transport and morphological change in the swash zone of a high-energy
1480 sandy beach from swash event to tidal cycle time scales. *Marine Geology*
1481 267 (1-2), 18–35.
- 1482 McLean, S. R., Ribberink, J. S., Dohmen-Janssen, C. M., Hassan, W. N.,
1483 2001. Sand transport in oscillatory sheet flow with mean current. *Journal*
1484 *of Waterway, Port, Coastal, and Ocean Engineering* 127 (3), 141–151.
- 1485 Mieras, R. S., Puleo, J. A., Anderson, D., Cox, D. T., Hsu, T.-J., 2017. Large-
1486 scale experimental observations of sheet flow on a sandbar under skewed-
1487 asymmetric waves. *Journal of Geophysical Research: Oceans* 122 (6), 5022–
1488 5045.

- 1489 O'Donoghue, T., Kikkert, G. A., Pokrajac, D., Dodd, N., Briganti, R.,
1490 2016. Intra-swash hydrodynamics and sediment flux for dambreak swash
1491 on coarse-grained beaches. *Coastal Engineering* 112, 113–130.
- 1492 O'Donoghue, T., Pokrajac, D., Hondebrink, L. J., 2010. Laboratory and
1493 numerical study of dambreak-generated swash on impermeable slopes.
1494 *Coastal Engineering* 57 (5), 513–530.
- 1495 O'Donoghue, T., Wright, S., 2004a. Concentrations in oscillatory sheet flow
1496 for well sorted and graded sands. *Coastal Engineering* 50 (3), 117–138.
- 1497 O'Donoghue, T., Wright, S., 2004b. Flow tunnel measurements of velocities
1498 and sand flux in oscillatory sheet flow for well-sorted and graded sands.
1499 *Coastal Engineering* 51 (11-12), 1163–1184.
- 1500 Osborne, P. D., Rooker, G. A., 1999. Sand re-suspension events in a high
1501 energy infragravity swash zone. *Journal of Coastal Research* 15 (1), 74–86.
- 1502 Othman, I. K., Baldock, T. E., Callaghan, D. P., 2014. Measurement and
1503 modelling of the influence of grain size and pressure gradient on swash
1504 uprush sediment transport. *Coastal Engineering* 83, 1–14.
- 1505 Padilla, E. M., Alsina, J. M., 2017. Transfer and dissipation of energy during
1506 wave group propagation on a gentle beach slope. *Journal of Geophysical*
1507 *Research: Oceans* 122 (8), 6773–6794.
- 1508 Padilla, E. M., Alsina, J. M., 2018. Long wave generation induced by differ-
1509 ences in the wavegroup structure. *Journal of Geophysical Research: Oceans*
1510 123 (12), 8921–8940.

- 1511 Peregrine, D. H., 1974. Water-wave interactions in the surf zone. In: Proceed-
1512 ings of 14th Conference on Coastal Engineering, Copenhagen Denmark. pp.
1513 500–517.
- 1514 Pintado-Patiño, J. C., Torres-Freyermuth, A., Puleo, J. A., Pokrajac, D.,
1515 2015. On the role of infiltration and exfiltration in swash zone boundary
1516 layer dynamics. *Journal of Geophysical Research: Oceans* 120 (9), 6329–
1517 6350.
- 1518 Postacchini, M., Brocchini, M., Mancinelli, A., Landon, M., 2012. A multi-
1519 purpose, intra-wave, shallow water hydro-morphodynamic solver. *Ad-
1520 vances in Water Resources* 38, 13–26.
- 1521 Postacchini, M., Othman, I. K., Brocchini, M., Baldock, T. E., 2014. Sed-
1522 iment transport and morphodynamics generated by a dam-break swash
1523 uprush: Coupled vs uncoupled modeling. *Coastal Engineering* 89, 99–105.
- 1524 Pritchard, D., Hogg, A. J., 2005. On the transport of suspended sediment by
1525 a swash event on a plane beach. *Coastal Engineering* 52 (1), 1–23.
- 1526 Pujara, N., Liu, P. L. F., Yeh, H., 2015a. The swash of solitary waves on a
1527 plane beach: flow evolution, bed shear stress and run-up. *Journal of Fluid
1528 Mechanics* 779, 556–597.
- 1529 Pujara, N., Liu, P. L. F., Yeh, H. H., 2015b. An experimental study of
1530 the interaction of two successive solitary waves in the swash: A strongly
1531 interacting case and a weakly interacting case. *Coastal Engineering* 105,
1532 66–74.

- 1533 Puleo, J. A., Beach, R. A., Holman, R. A., Allen, J. S., 2000. Swash zone
1534 sediment suspension and transport and the importance of bore-generated
1535 turbulence. *Journal of Geophysical Research* 105 (C7), 17021.
- 1536 Puleo, J. A., Krafft, D., Pintado-Patiño, J. C., Bruder, B., 2017. Video-
1537 derived near bed and sheet flow sediment particle velocities in dam-break-
1538 driven swash. *Coastal Engineering* 126, 27–36.
- 1539 Puleo, J. A., Lanckriet, T., Blenkinsopp, C., 2014. Bed level fluctuations in
1540 the inner surf and swash zone of a dissipative beach. *Marine Geology* 349,
1541 99–112.
- 1542 Puleo, J. A., Lanckriet, T., Conley, D., Foster, D., 2016. Sediment transport
1543 partitioning in the swash zone of a large-scale laboratory beach. *Coastal*
1544 *Engineering* 113, 73–87.
- 1545 Ribberink, J. S., Al-Salem, A. A., 1995. Sheet flow and suspension of sand
1546 in oscillatory boundary-layers. *Coastal Engineering* 25 (3-4), 205–225.
- 1547 Ruffini, G., Briganti, R., Alsina, J. M., Brocchini, M., Dodd, N., McCall, R.,
1548 2019. Numerical modelling of flow and bed evolution of bichromatic wave
1549 groups on an intermediate beach using non-hydrostatic xbeach. *Journal of*
1550 *Waterway Port Coastal and Ocean Engineering* in press.
- 1551 Ruju, A., Conley, D., Masselink, G., Puleo, J., 2016. Sediment transport
1552 dynamics in the swash zone under large-scale laboratory conditions. *Con-*
1553 *tinental Shelf Research* 120, 1–13.
- 1554 Sánchez-Arcilla, A., Cáceres, I., 2017. An analysis of nearshore profile and

- 1555 bar development under large scale erosive and accretive waves. *Journal of*
1556 *Hydraulic Research* 56 (2), 231–244.
- 1557 Schretlen, J., 2012. Sand transport under full-scale progressive surface waves.
1558 Phd thesis, University of Twente, The Netherlands.
- 1559 Shen, M. C., Meyer, R. E., 1963. Climb of a bore on a beach part 3. run-up.
1560 *Journal of Fluid Mechanics* 16 (01), 113.
- 1561 Sou, I. M., Yeh, H., 2011. Laboratory study of the cross-shore flow structure
1562 in the surf and swash zones. *Journal of Geophysical Research* 116 (C3).
- 1563 Sumer, B. M., Kozakiewicz, A., Fredsoe, J., Deigaard, R., 1996. Velocity
1564 and concentration profiles in sheet-flow layer of movable bed. *Journal of*
1565 *Hydraulic Engineering* 122 (10), 549–558.
- 1566 Symonds, G., Huntley, D. A., Bowen, A. J., 1982. Two-dimensional surf beat:
1567 Long wave generation by a time-varying breakpoint. *Journal of Geophys-*
1568 *ical Research* 87 (C1), 492.
- 1569 Tissier, M., Bonneton, P., Michallet, H., Ruessink, B. G., 2015. Infragravity-
1570 wave modulation of short-wave celerity in the surf zone. *Journal of Geo-*
1571 *physical Research: Oceans* 120 (10), 6799–6814.
- 1572 Torres-Freyermuth, A., Puleo, J. A., Pokrajac, D., 2013. Modeling swash-
1573 zone hydrodynamics and shear stresses on planar slopes using reynolds-
1574 averaged navier-stokes equations. *Journal of Geophysical Research: Oceans*
1575 118 (2), 1019–1033.

- 1576 van der Zanden, J., Alsina, J. M., Cáceres, I., Buijsrogge, R. H., Ribberink,
1577 J. S., 2015. Bed level motions and sheet flow processes in the swash zone:
1578 Observations with a new conductivity-based concentration measuring tech-
1579 nique (ccm+). *Coastal Engineering* 105, 47–65.
- 1580 van der Zanden, J., van der A, D. A., Cáceres, I., Larsen, B. E., Fromant, G.,
1581 Petrotta, C., Scandura, P., Li, M., 2019. Spatial and temporal distributions
1582 of turbulence under bichromatic breaking waves. *Coastal Engineering* 146,
1583 65–80.
- 1584 van der Zanden, J., van der A, D. A., Hurther, D., Cáceres, I., O’Donoghue,
1585 T., Hulscher, S. J. M. H., Ribberink, J. S., 2017. Bedload and suspended
1586 load contributions to breaker bar morphodynamics. *Coastal Engineering*
1587 129, 74–92.
- 1588 van Dongeren, A., Battjes, J., Janssen, T., van Noorloos, J., Steenhauer, K.,
1589 Steenbergen, G., Reniers, A., 2007. Shoaling and shoreline dissipation of
1590 low-frequency waves. *Journal of Geophysical Research* 112 (C2).
- 1591 van Rijn, L. C., 2007. Unified view of sediment transport by currents and
1592 waves. i: Initiation of motion, bed roughness, and bed-load transport.
1593 *Journal of Hydraulic Engineering-Asce* 133 (6), 649–667.
- 1594 van Rijn, L. C., Ribberink, J. S., van der Werf, J. J., Walstra, D. J. R., 2013.
1595 Coastal sediment dynamics: recent advances and future research needs.
1596 *Journal of Hydraulic Research* 51 (5), 475–493.
- 1597 Wang, Y.-H., Yu, G.-H., 2007. Velocity and concentration profiles of particle
1598 movement in sheet flows. *Advances in Water Resources* 30 (5), 1355–1359.

- 1599 Weir, F. M., Hughes, M. G., Baldock, T. E., 2006. Beach face and berm
1600 morphodynamics fronting a coastal lagoon. *Geomorphology* 82 (3-4), 331–
1601 346.
- 1602 Wilson, K. C., 1966. Bed-load transport at high shear stress. *Journal of the*
1603 *Hydraulics Division* 92 (6), 49–59.
- 1604 Wu, L., Feng, D., Shimosono, T., Okayasu, A., 2016. Laboratory measure-
1605 ments of sediment flux and bed level evolution in the swash zone. *Coastal*
1606 *Engineering Journal* 58 (02), 1650004.
- 1607 Zhu, F., Dodd, N., 2013. Net beach change in the swash zone: A numerical
1608 investigation. *Advances in Water Resources* 53, 12–22.
- 1609 Zhu, F. F., Dodd, N., 2015. The morphodynamics of a swash event on an
1610 erodible beach. *Journal of Fluid Mechanics* 762, 110–140.

Table 1: Positions of instruments in the swash zone. Vertical positions with respect to the bed level at the start of each experimental run are only given when relevant.

Instrument	x (m)	$z - z_{\text{bed}}$ (m)
CCM ⁺	1.28 (tank 1), -0.52 (tank 2)	
ADV _s	-1.54, -0.52, 0.27, 1.28, 2.26	0.03
OBS _s	-1.68, -0.45, 0.38, 1.28, 2.36	0.03
PT _s	1.23, 1.28, 1.33	-0.01
AWG _s	-1.57, -0.52, 0.47, 1.25, 2.31, 3.5, 4.55, 5.56, 6.51	

Table 2: Magnitudes of sand transport rates and bed level changes in the lower swash zone, and relative significance of sediment exchange across the surf-swash boundary compared to sediment mobilized within the swash zone, at different time scales.

Time scale	q_{tot} (kg/ms)	$\Delta z_{\text{bed}}/\Delta t$ (mm/s)	Δz_{bed} (mm)	Significance surf-swash exchange
Intra-swash	1 to 10	1 to 15	2 to 20	Low
Integrated over one swash event	0.1 to 0.5	0.1 to 0.5	2 to 8	Moderately low
Integrated over both events	0.01 to 0.05	0.005 to 0.02	0.05 to 1	High
Integrated over 60-min run	0.01 to 0.05	0.005 to 0.02	10 to 50	High

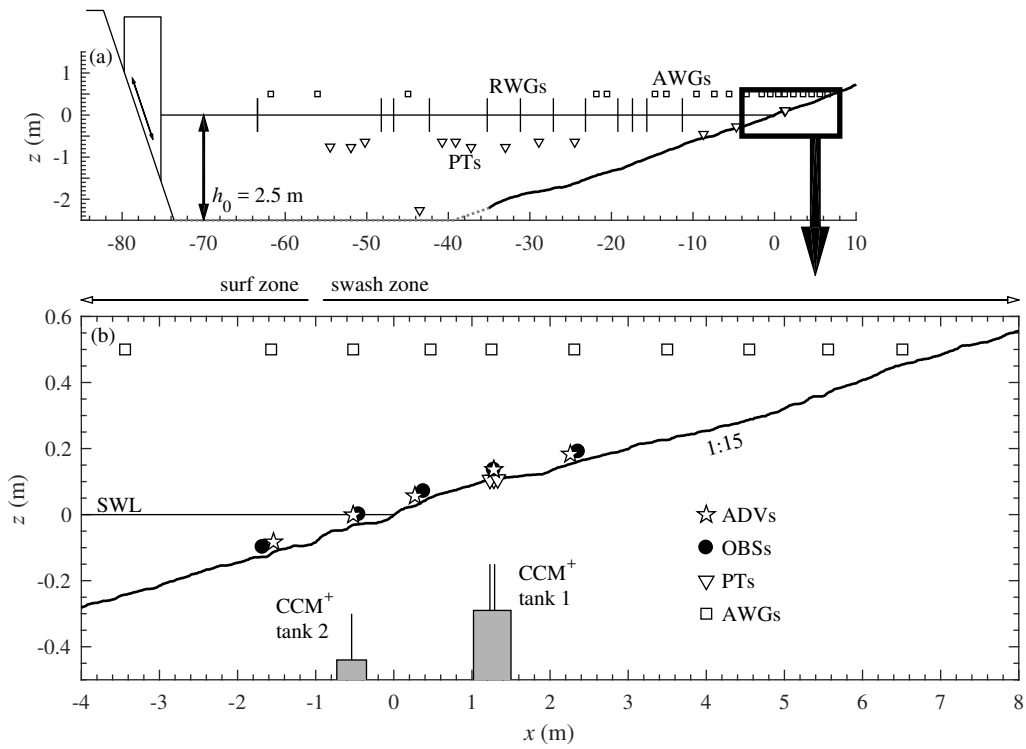


Figure 1: Experimental set-up: initial 1:15 sloping bed and position of instruments.

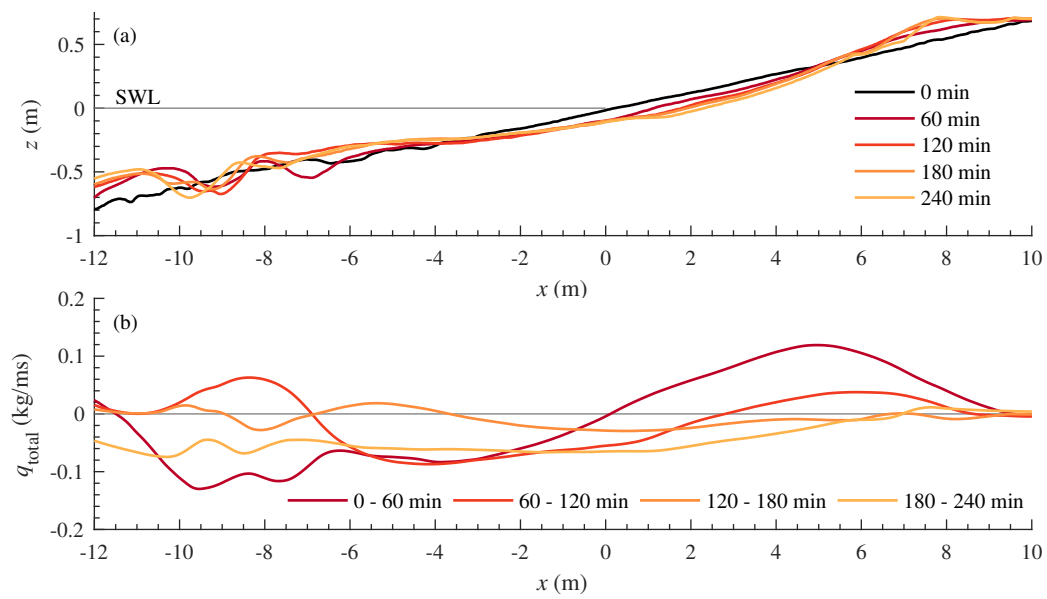


Figure 2: (a) Bed profile evolution; (b) Net sand transport rates obtained through Equation 1.

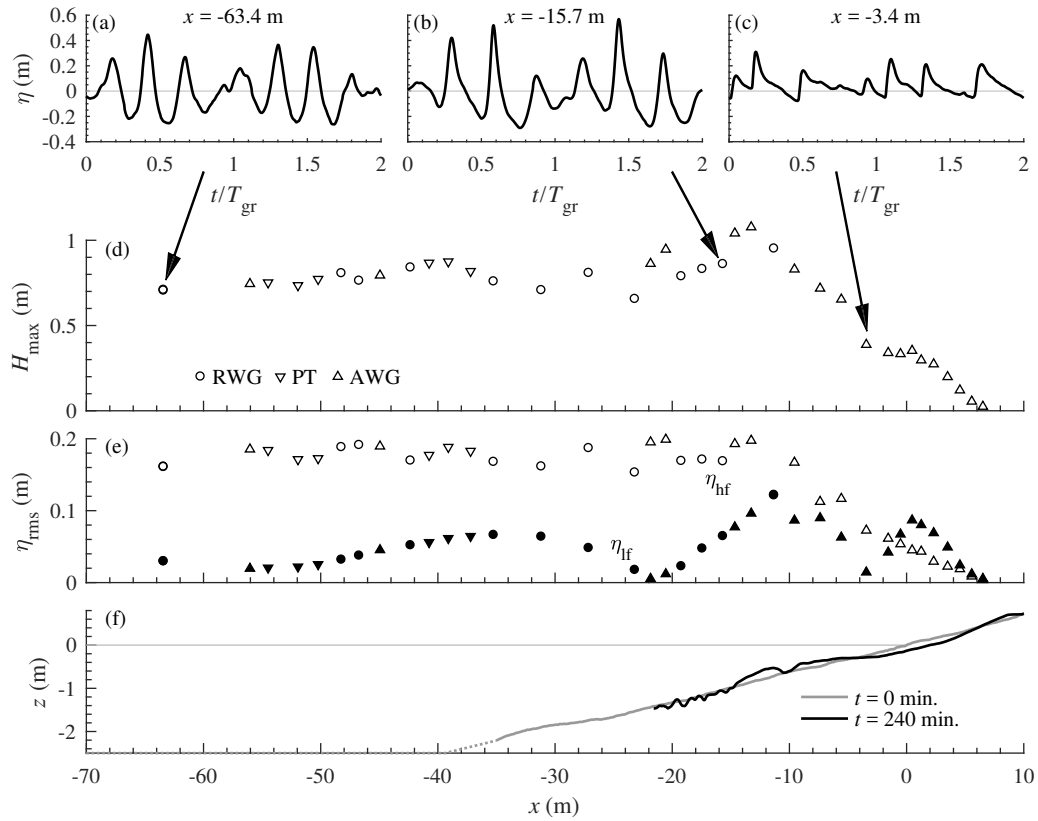


Figure 3: (a, b, c) Time series of phase-averaged water surface elevation at three locations; (d) $H_{max} = \eta_{max} - \eta_{min}$, measured with RWGs (circles), pressure transducers (downward triangles) and acoustic wave gauges (upward triangles); (e) root-mean-square high-pass (“hf”, open markers) and low-pass (“lf”, solid markers) filtered water surface elevation, corresponding to short waves and wave groups, respectively; (f) initial (grey) and final (black) bed profile.

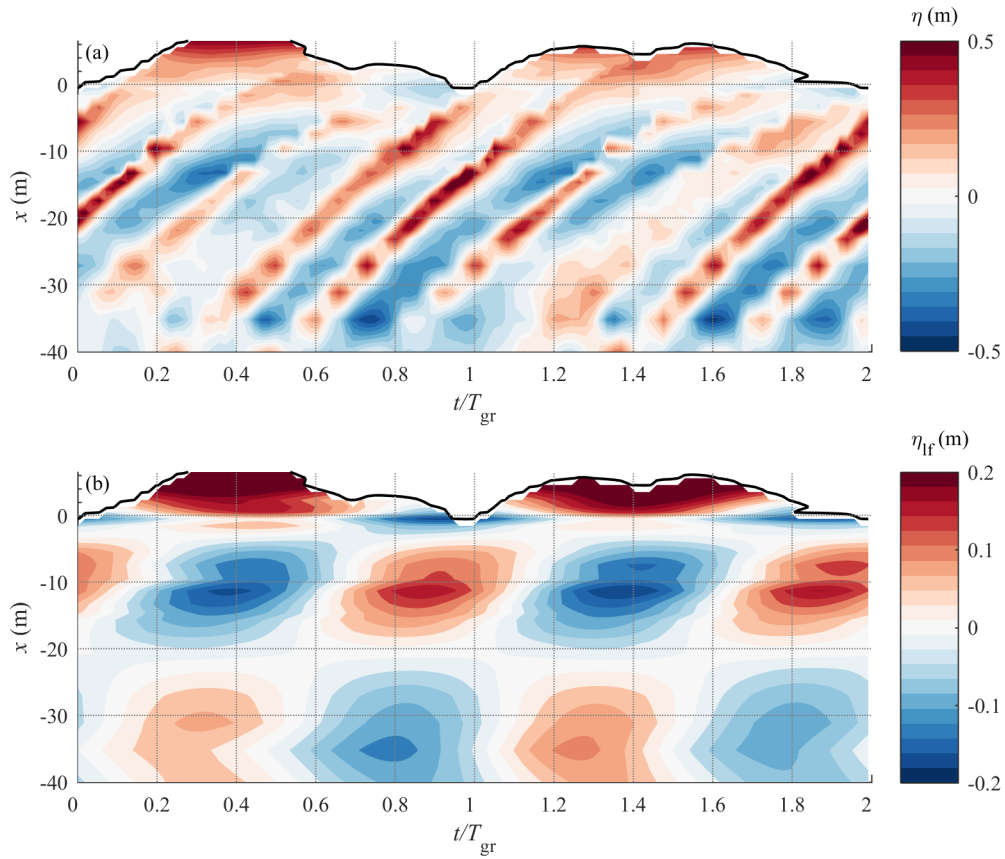


Figure 4: Colour contour of the phase-averaged water surface elevation along the entire flume: (a) η , (b) η_f . The solid black line is the $h = 0.01$ m iso-line, highlighted here as a proxy for the shoreline.

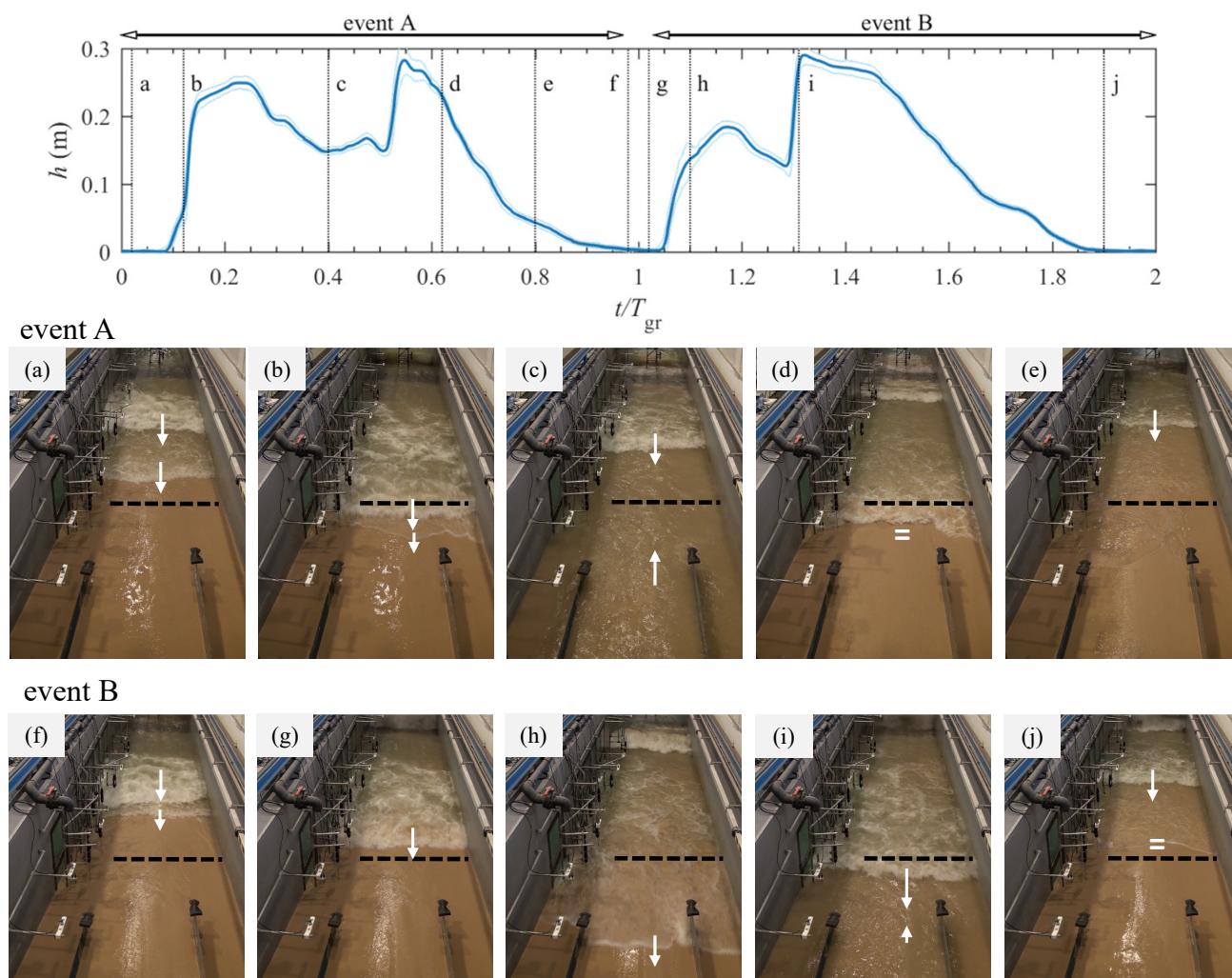


Figure 5: Top panel: time series of the phase-averaged water depth at $x = 1.25$ m (location corresponding to CCM⁺ tank 1), measured by AWG (solid line: ensemble-mean; dashed lines: \pm one standard deviation). Lower panels show snapshots of a video recording (a-j) with reference to time instants in upper panel. The black dashed line in the photos marks the location of the water surface measurement in the top panel; the white arrows mark the direction of incident bores and the backwash flow.

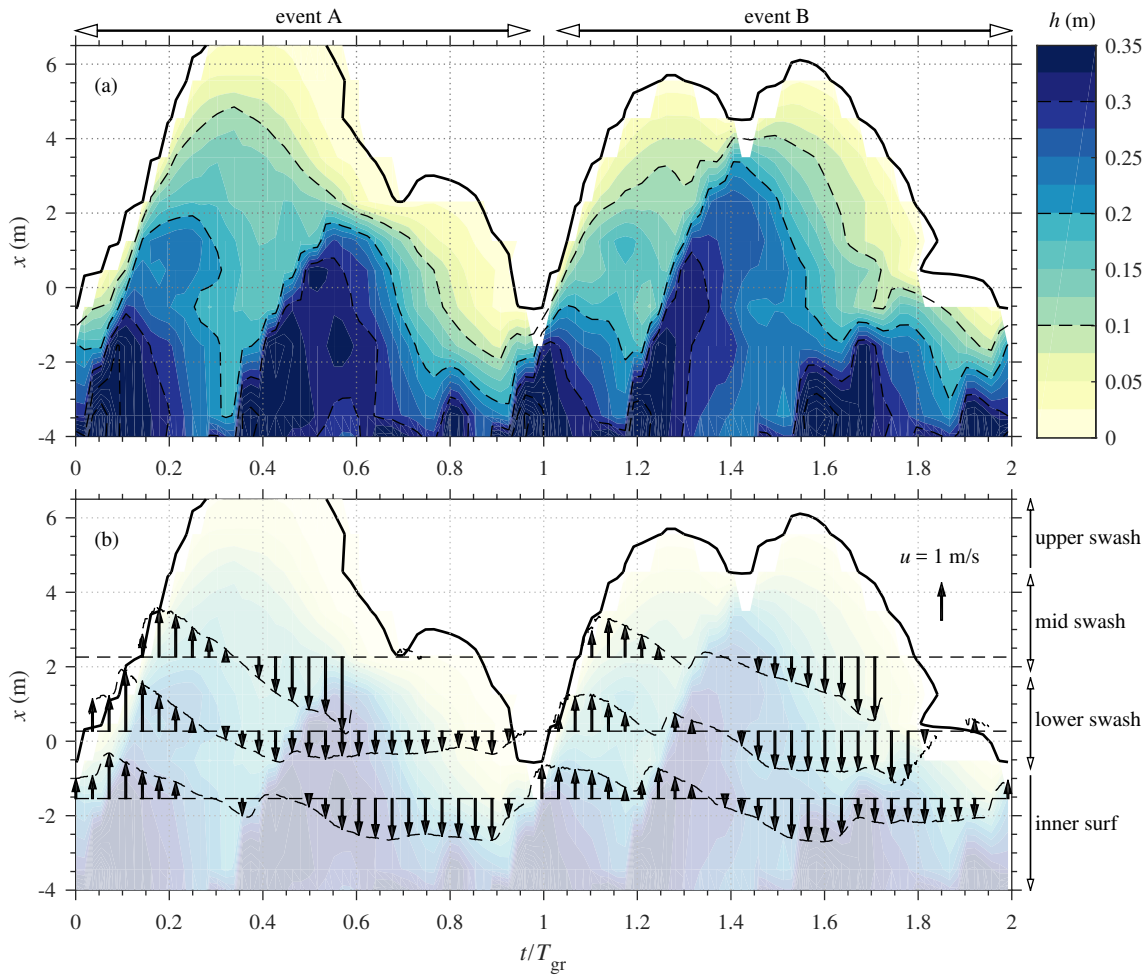


Figure 6: (a) Colour contour of water depth in swash zone; thick solid line denotes the $h = 0.01$ m isoline (proxy for instantaneous shoreline location), dashed lines denote the $h = 0.10, 0.20,$ and 0.30 m isolines; (b) As (a), but with the cross-shore velocity at three cross-shore locations superimposed as vectors.

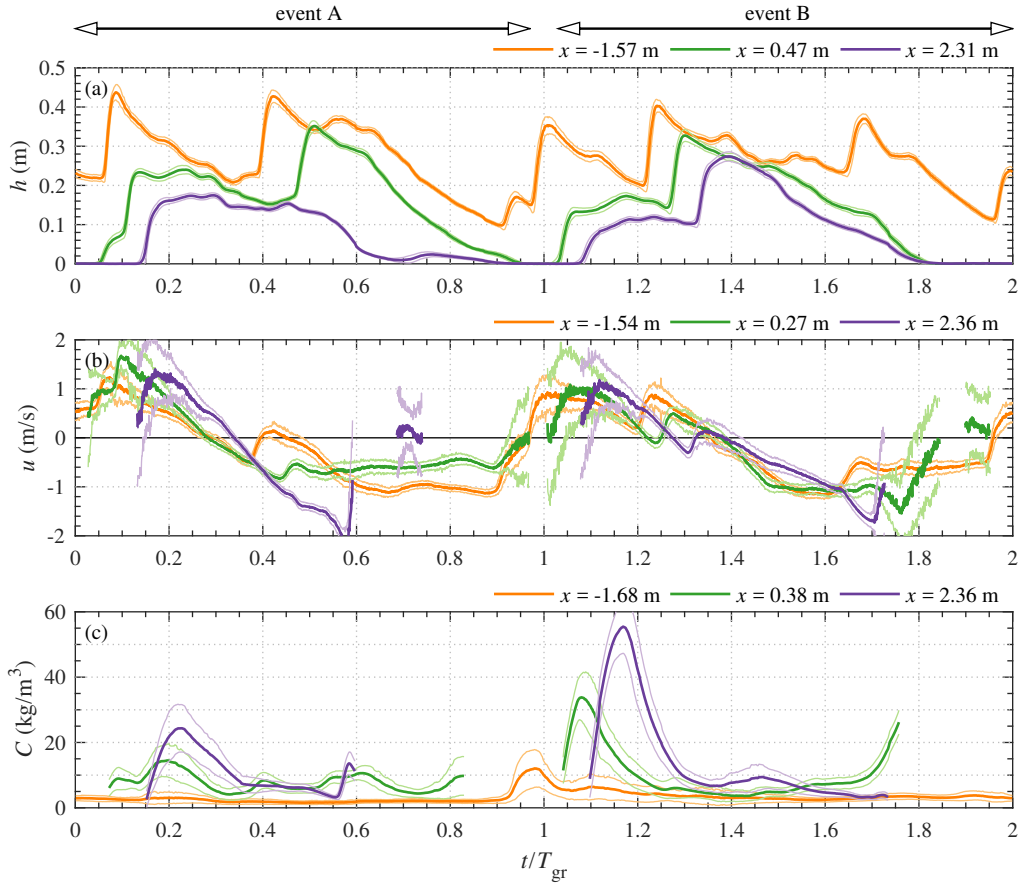


Figure 7: Water depth (a), cross-shore velocity (b) and suspended sand concentration (c) at three cross-shore locations in the swash zone. Velocity and sand concentration were measured at $z - z_{\text{bed}} = 0.03$ m. Thick line represents the ensemble-mean, thin lines mark \pm standard deviation.

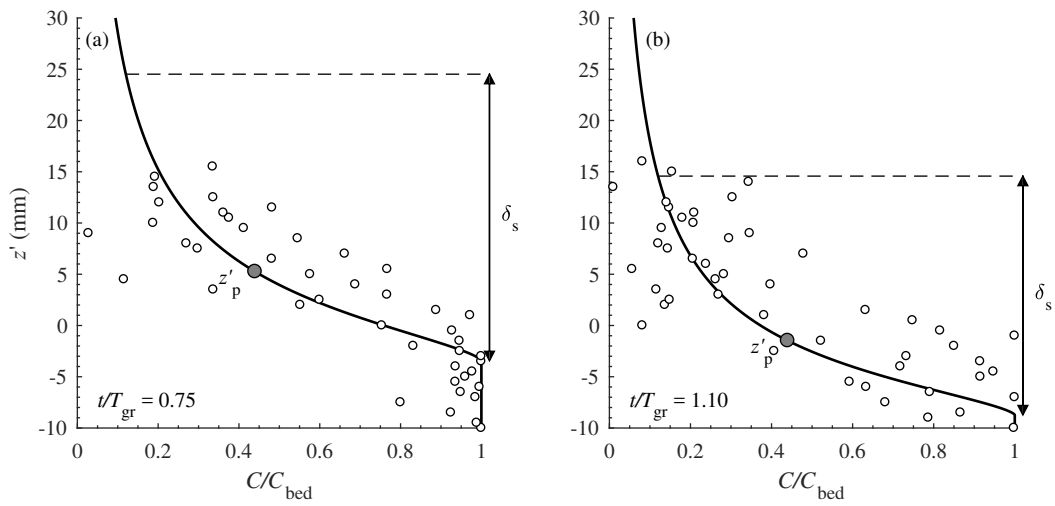


Figure 8: Illustration of Equation 2 (O'Donoghue and Wright, 2004a) fit to CCM⁺ concentration measurements. White circles mark the measured $C(z, t/T_{gr})$ at $x = 1.28$ m. Solid black line represents the fit, the grey circle marks the elevation of the sheet flow layer pivot point.

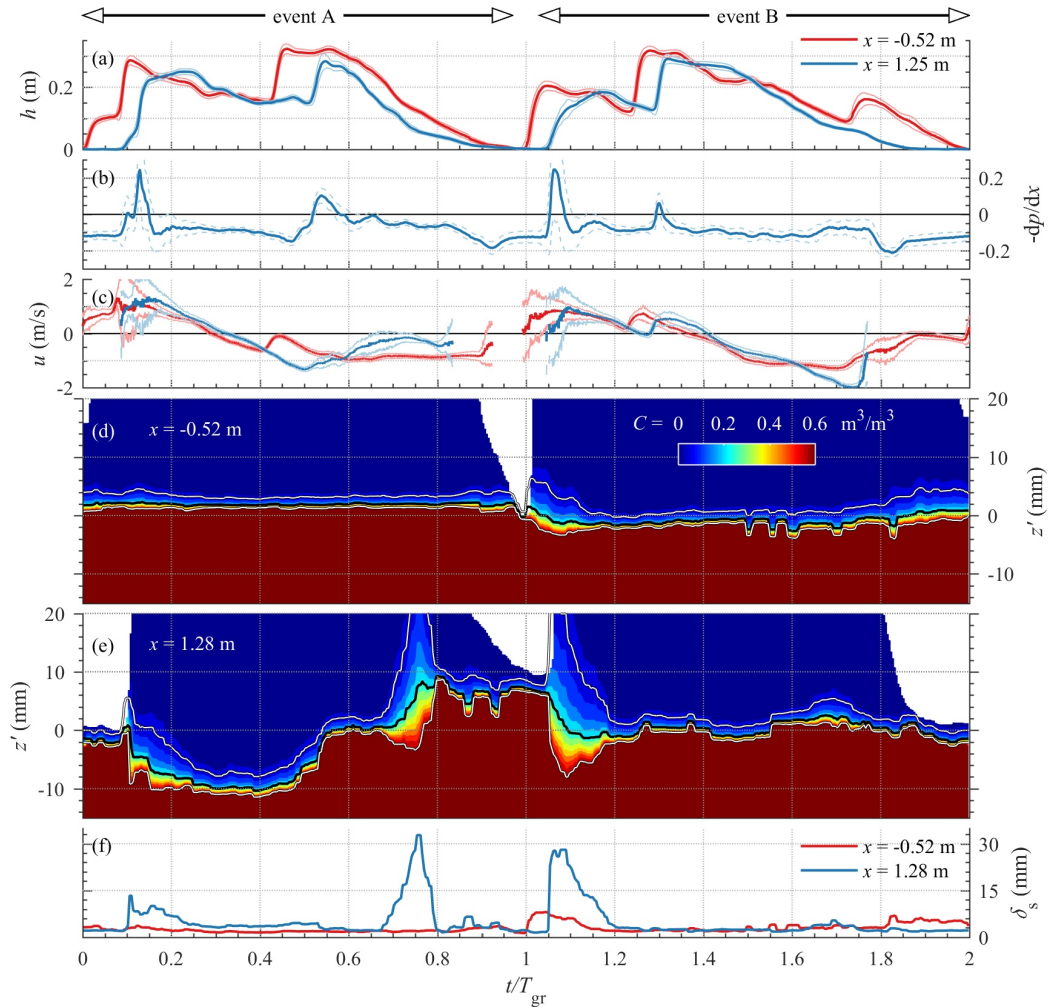


Figure 9: Phase-averaged hydrodynamics and sheet flow dynamics at the two CCM⁺ locations in the lower swash zone. (a) Water depths (mean +/- standard deviation); (b) Cross-shore pressure gradients at the location of CCM⁺ tank 1 (mean +/- standard deviation); (c) Cross-shore velocities (mean +/- standard deviation); (d, e) Vertical distribution of concentrations in the sheet flow layer, obtained by Equation 2 fit to CCM⁺ measurements. Solid black line denotes the sheet flow layer pivot point, white lines mark the sheet flow layer top and bottom; (f) Sheet flow layer thickness at both locations.

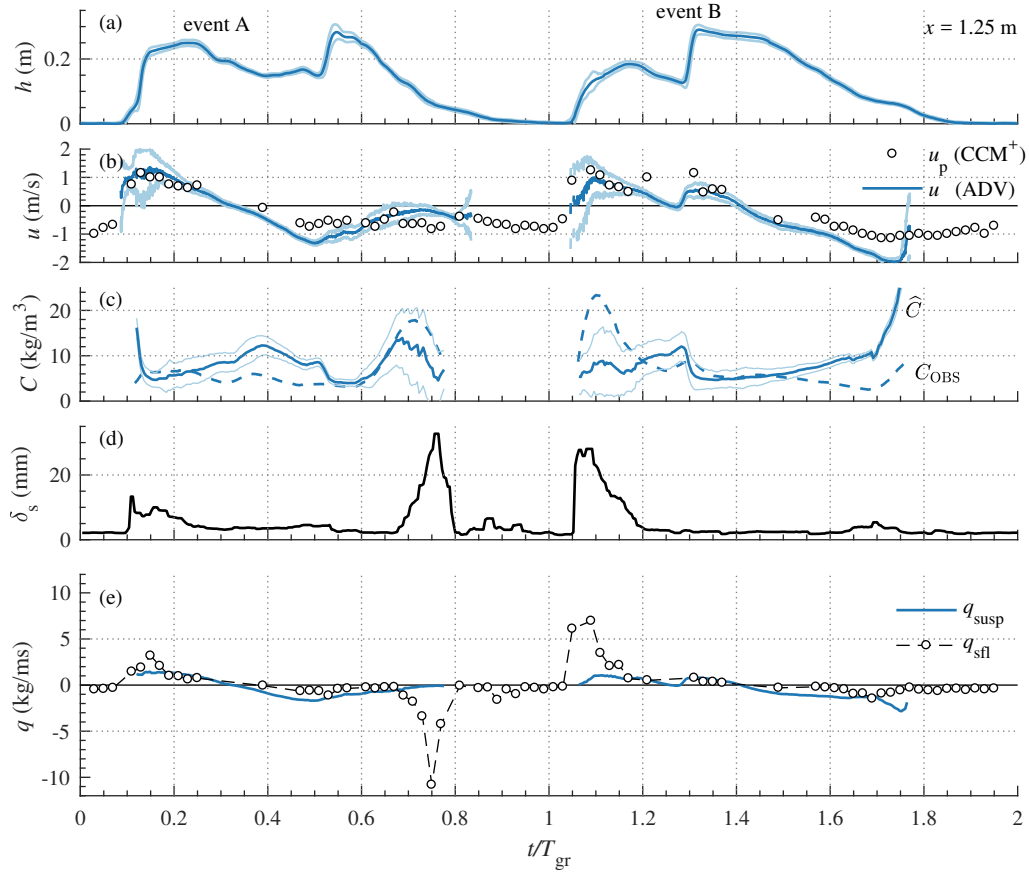


Figure 10: Depth-integrated transport rates at the location of CCM⁺ tank 1 ($x = 1.28$ m). (a). Water depth; (b) Flow velocity measured by ADV at $z - z_{\text{bed}} = 0.03$ m (solid lines; mean \pm standard deviation) and particle velocity measured by CCM⁺ at the top of the sheet flow layer (circles); (c) Suspended sand concentration, measured by OBS at $z - z_{\text{bed}} = 0.03$ m (dashed) and depth-averaged following Equation 7 (solid); (d) Sheet flow layer thickness; (e) Depth-integrated suspended (blue solid line) and sheet flow layer (circles and dashed line) sand transport rates.

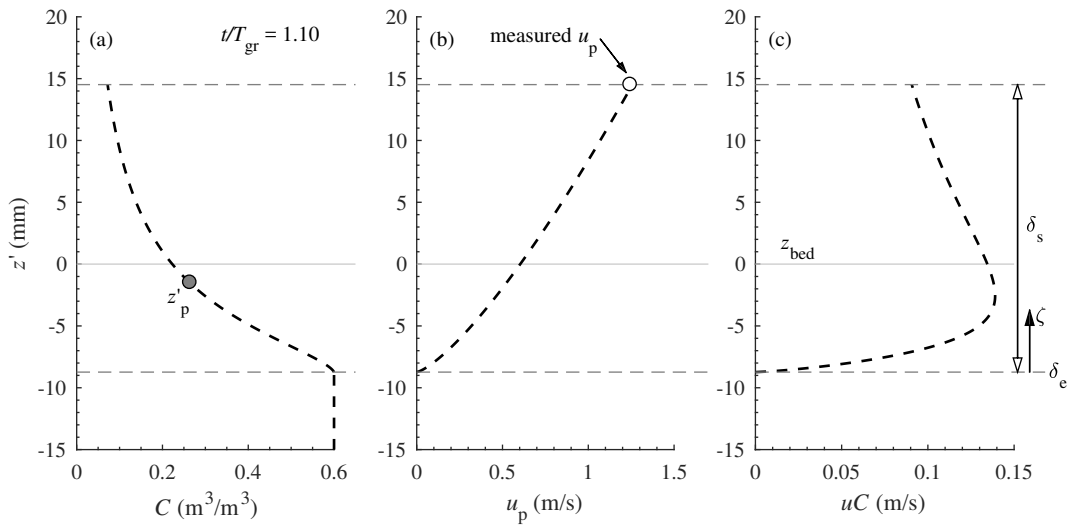


Figure 11: Illustration of sheet flow sand flux calculations. (a) Concentration profile (Equation 2); (b) Vertical profile of the cross-shore velocity: the circle shows the measured particle velocity by the CCM⁺, dashed line shows the distribution following Equation 8; (c) Resulting flux distribution $\phi = uC$.

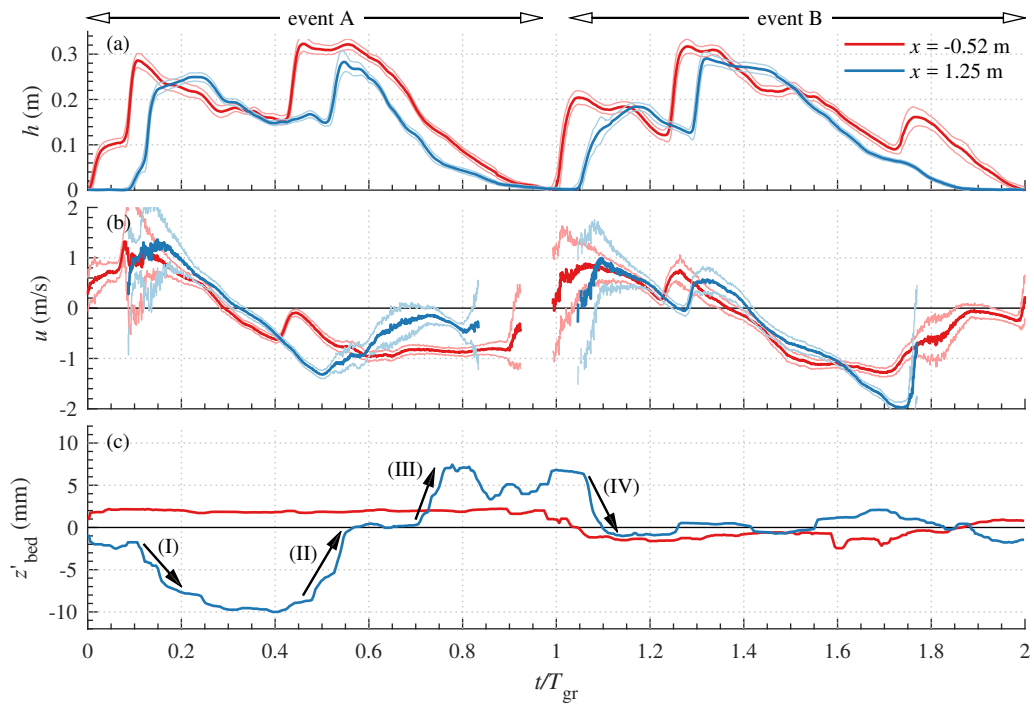


Figure 12: Intra-swash hydrodynamics and bed level at both CCM⁺ locations (blue: CCM⁺ tank 1, red: tank 2). (a) Water depths; (b) Velocity; (c) Bed level measurements by CCM⁺, with I-IV indicating pick-up and deposition events that are discussed in the main text.

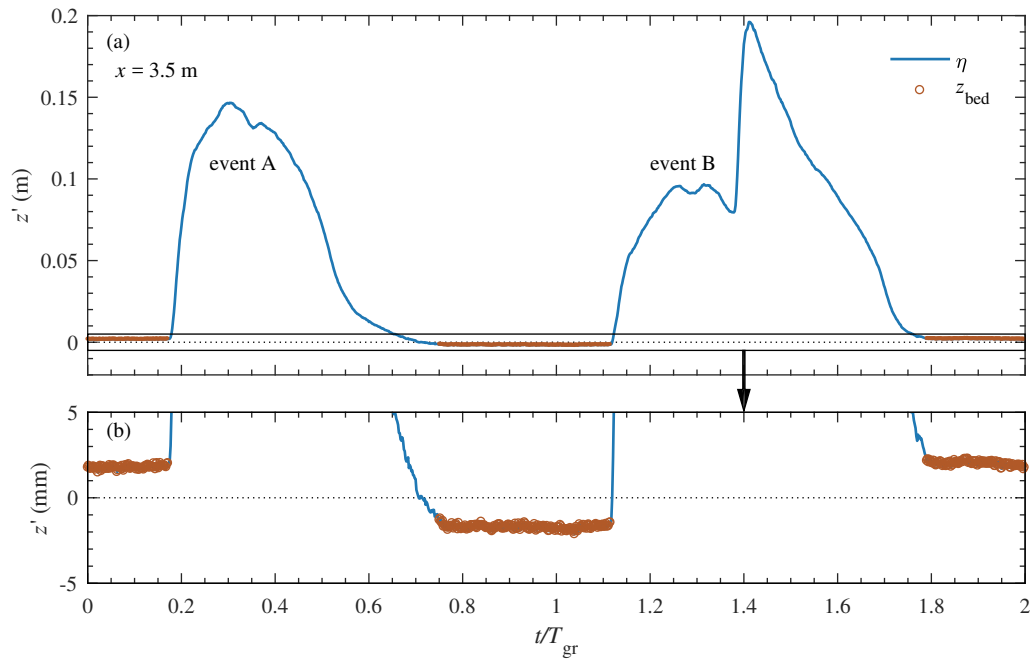


Figure 13: Illustration of bed level measurement by AWG: blue solid lines show the phase-averaged AWG measurement, brown circles show the identified exposed bed level. (b) shows a close-up of (a).

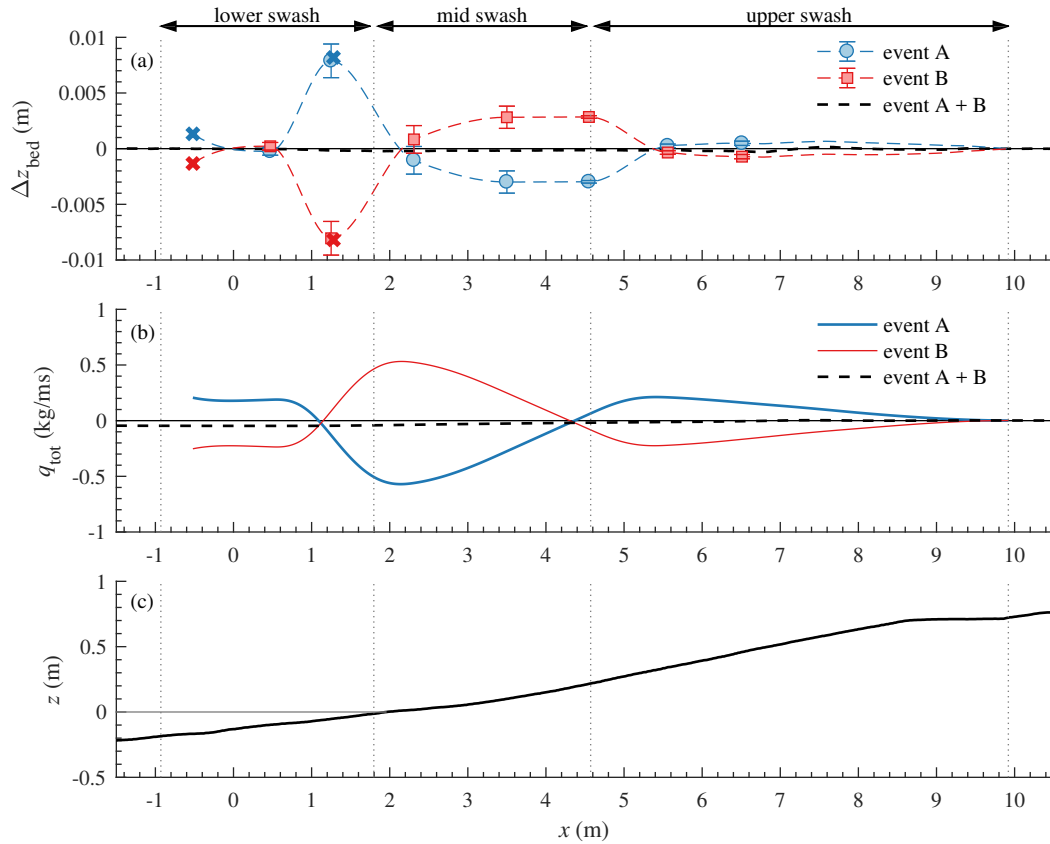


Figure 14: (a) Net bed level change by swash events A (blue) and B (red), measured by AWG (circles: event A; squares: event B) and CCM⁺ (crosses), and cubic interpolation of the measurements (dashed lines); (b) Mean sand transport rates over events A (blue) and B (red), calculated from the net bed level changes, and the mean sand transport rate over both events obtained from the bed profile measurements (black dashed; previously also shown in Figure 2b); (c) Final bed profile.